RESEARCH ARTICLE

# Does the topographic data source truly influence the routing modelling of debris flows in a torrent catchment?

Mauro Boreggio | Martino Bernard | Carlo Gregoretti

Department of Land, Environment, Agriculture and Forestry (TeSAF), University of Padova, Legnaro

**Correspondence**
Mauro Boreggio, Department of Land, Environment, Agriculture and Forestry (TeSAF), University of Padova, Legnaro, Italy.
Email: mauro.boreggio@unipd.it

## Abstract

To cope with debris-flow hazards, a common practice is the mapping of threatened areas through routing models. Considering the primary role of topography in affecting the mobility of gravity-driven flows, its proper representation through digital elevation models (DEMs) is a requirement in routing modelling applications. The 'quality' of DEMs mainly depends on the quality, resolution and spatial arrangement of the topographic measurements (i.e. on the employed survey technology). Nevertheless, no attempt to systematically evaluate the influence of the topographic data source on the behaviour of routing models has been carried out. To address this, we initially assess the performances of both terrestrial- (i.e. global navigation satellite system, GNSS) and airborne-based (i.e. full-waveform LiDAR and structure-from-motion, SfM digital photogrammetry) survey technologies in characterizing the topography of a debris-flow channel. Afterwards, we investigate whether the topographic data source can effectively influence the behaviour of a geographic information system (GIS)-based cell routing model. Regarding the assessment of the survey technologies performances, the 'standard' statistic-based approach indicated that GNSS and full-waveform LiDAR can provide an accurate digital representation of the gully. However, the analysis of the shapes stressed that the most faithful and finer reproduction of the topographic singularities is yielded by the photogrammetrically reconstructed surface due to the extremely high data source resolution. Furthermore, the pairwise comparison of derived elevation models pointed out that meaningful discrepancies among tested survey technologies can be detected in morphologically complex areas because of the inherent limits of the terrestrial-based method. Here, this research showed how these discrepancies have the potential to affect simulated flow dynamics, even if not in a meaningful way from a risk planning and management point of view. Overall, it appears that the topographic data source does not truly represent a determining factor in modelling applications of channelized debris-flow routing.

**KEYWORDS**
alpine gully, debris-flow routing modelling, DEM elevation quality assessment, DEM elevation uncertainty modelling, DEM of Difference (DoD), Digital Elevation Model (DEM), digital photogrammetry, Global Navigation Satellite System (GNSS), stony debris flows, survey technologies comparison

# 1 | INTRODUCTION

According to the original definition proposed by Takahashi (1981), in-channel debris flows can be described as massive sediment transport phenomena that occur in mountain streams characterized by steep slopes, wherein the motion of the granular phase is directly induced by gravity and the ratio between the liquid and solid transport rates is relatively low.

Among the geomorphic processes occurring in steep headwater basins, debris flows can be regarded as one of the most hazardous phenomena due to their magnitude, routing velocity and high occurrence rate in a wide spectrum of morphological settings (e.g. Hurlimann et al., 2006). To cope with this natural hazard, a common practice is the mapping of the areas historically or potentially threatened (Ghilardi et al., 2001) by adopting an empirical (e.g. Berti & Simoni, 2014; Scheidl & Rickenman, 2010) or model-based (e.g. Armanini et al., 2009; Frank et al., 2015; Gregoretti et al., 2019; Hussin et al., 2012; Medina et al., 2008) approach. In the latter case, since the motion of gravity-driven flows is extremely sensitive to topographic changes (e.g. abrupt slope discontinuities, obstacles or ravine deviations; Capra et al., 2011; Rickenmann et al., 2006), the proper representation of the real channel and fan morphology through digital elevation models (DEMs, also known as digital terrain models or DTMs) is essential for the reliability of debris-flow routing modelling outcomes. In fact, the DEM represents the most important input in debris flow routing models (e.g. Rickenmann et al., 2006; Sodnik et al., 2012), and from a mathematical point of view it is simply a function $z = f(p_{x,y})$ mapping a unique height value (referred to the bare earth) to each planimetric location $p_{x,y}$ (Briese in Vosselman & Maas, 2010; Pfeifer, 2005).

A DEM is always generated starting from a collected topographic dataset (e.g. points and lines) by means of deterministic or stochastic gridding algorithms (Hengl & Reuter, 2009). The topographic data acquisition method for digital terrain modelling purposes usually depends on the application (e.g. reach-scale flood modelling), and on its specific requirements in terms of both data quality and density (Höhle & Potuckova, 2011). In the past, analytical aerial photogrammetry along with classic terrestrial-based topographic surveys were the main measurement methods for collecting topographic information on areas featuring different extensions. In the last two decades, sensor modernization has promoted the development of new and highly automated remote-sensing technologies, such as airborne- and terrestrial-based laser scanning (ALS and TLS, respectively), long- and close-range digital photogrammetry and interferometric synthetic aperture radar (e.g. Höhle & Potuckova, 2011; Hsieh et al., 2016; Jaboyedoff et al., 2012; Lillesand et al., 2004; Molina et al., 2014; Westoby et al., 2012). All these new survey technologies have the capability to acquire high-resolution topographic data (i.e. metre and submetre posts-spacing) within a short time and with a high-quality level. Nevertheless, classic terrestrial-based surveys by means of a global navigation satellite system (GNSS) or total stations have not been completely set aside since they ensure a proper trade-off between quality and cost for scenarios involving small areas without the need for massive topographic data acquisition (Casas et al., 2006; Gomarasca, 2009).

Considering the wide range of satellite-, airborne- and terrestrial-based survey technologies currently available and their

inherent limitations (which result in trade-offs among cost, quality, resolution, spatial coverage and sampling frequency), the choice of the proper survey method for a given application is not a trivial issue. For this reason, recent research efforts have been undertaken to investigate the main benefits and limitations of the available survey technologies under different conditions and environments (e.g. Bangen et al., 2014; Gallay et al., 2013; Molina et al., 2014; Passalacqua et al., 2015; Tarolli, 2014). In this context, several studies have also been carried out to explore the effects of topographic data sources on flood modelling outcomes (e.g. Alho et al., 2009; Ali et al., 2015; Bakuła et al., 2016; Bhuyian & Kalyanapu, 2018; Casas et al., 2006; Cook & Merwade, 2009; Reil et al., 2017; Wilson & Atkinson, 2005; Table S1 in the online Supplementary Material). However, to date, little work has been performed to assess the performances of different terrestrial- and airborne-based survey technologies in morphologically complex and steep areas, such as those where debris flows occur. Furthermore, no attempt to evaluate the influence of the employed survey method on the behaviour of debris-flow routing models (i.e. numerical simulation outcomes) has been made.

To fill these research gaps, in this study we first assess and compare the performances of different terrestrial- (i.e. GNSS) and aerial-based (i.e. helicopter-based full-waveform LiDAR and unmanned aerial vehicle, UAV-based structure-from-motion, SfM digital photogrammetry) survey technologies widely used in the field of the numerical modelling of gravity-driven phenomena and suitable for characterizing the complex topography of a steep 1 km-length debris-flow channel reach located in the Venetian Dolomites (north-eastern Italian Alps). The investigation is performed by combining surface shape analysis, vertical quality assessment, spatially distributed modelling of vertical uncertainty and probabilistic differencing of (temporal concurrent) DEMs. Afterwards, we evaluate whether the resultant topographic characterization of the channel morphology can control the behaviour of a geographic information system (GIS)-based cell model suitable for simulating the propagation of stony debris flows by considering both high- and intermediate-magnitude flow conditions (i.e. 300- and 50-year return periods, respectively). In detail, we compare the outcomes of the model runs carried out using the different topographic surfaces by focusing on those concerning the hazard, which include: solid–liquid discharge hydrographs; areas inundated during the propagation; erosional–depositional volumes; and erosional–depositional depths, maximum flow depths and maximum thicknesses (defined as the sum of flow and depositional depths). Therefore, this research may represent a valuable contribution for digital elevation data users involved in debris-flow hazard assessment and mitigation at a basin or reach scale.

The paper is organized as follows. After this brief statement of the problem, the reader is provided with a detailed description of the study site, the available topographic datasets and the employed routing model. Then, all the applied procedures, from the interpolation of the elevation models to the assessment of the influence of the topographic data source on the outcomes of the employed routing model, are illustrated. The results and discussion summarize the obtained research outcomes. Finally, the conclusions complete the paper, highlighting the practical implications of the proposed research, along with its inherent limitations.
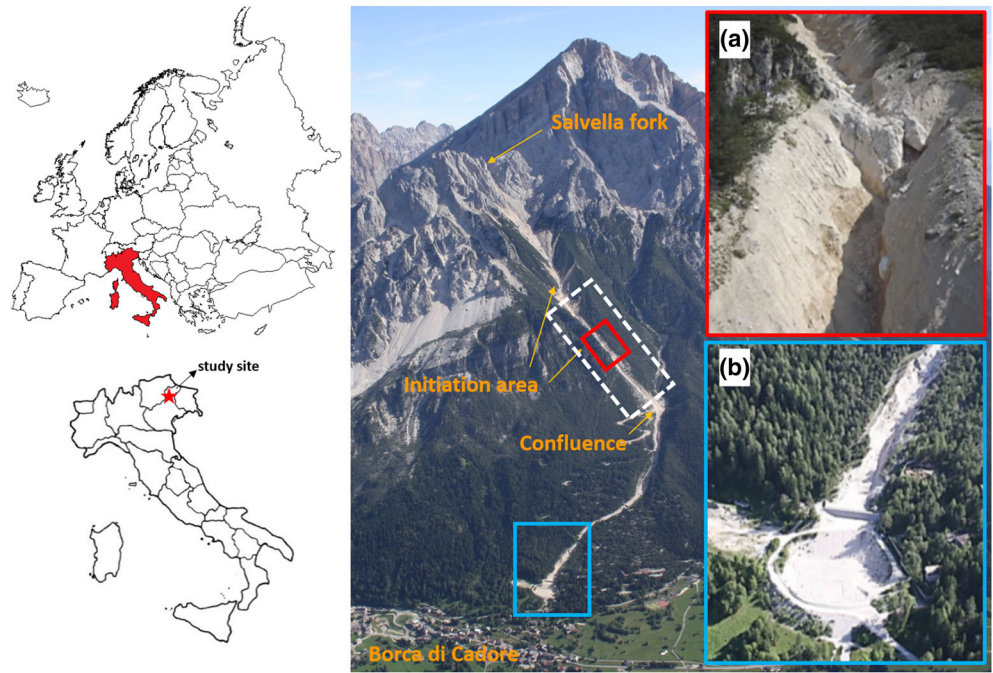
## 2 | MATERIALS

### 2.1 | Field site

The Rovina di Cancia debris-flow channel (Figure 1) originates in scree at the base of the Salvella fork (approximately 2450 m a.s.l.), and by extending downstream on the western slope of Mount Antelao, it ends within a flat circular depositional basin just upstream of the village of Borca di Cadore (approximately 1000 m a.s.l.). Notably, immediately downstream of a human-built depositional area (approximately 1340 m a.s.l.), on the left side, there is the intake of the Bus del Diau Creek, which mainly provides aliquid contribution to the main channel.

Rovina di Cancia debris flows usually initiate at approximately 1670 m a.s.l. since the gully bottom in its upper part mostly includes giant and large boulders hampering the formation of consistent solid–liquid waves (Bernard et al., 2019).

From a geomorphological point of view, three main sectors can be distinguished within the catchment. In the upper part, massive rock cliffs composed of Upper Triassic to Lower Jurassic dolomites and limestones, underlined by the Raibl Formation, prevail. The medium part is characterized by screes of poorly sorted and highly permeable debris, with boulders that can reach diameters of approximately 3–4 m. Finally, the lower part of the basin is covered by old debris-flow deposits, also including postglacial sediment material.

Overall, the study area is prone to stony debris flows due to both the availability of loose and coarse sediments and the impulsive hydrological regime. In particular, the smaller grain-sized material is provided by both the failure and the erosion of the channel banks, whereas gravel, pebbles and cobbles are provided by rockfalls mostly occurring in the upper part of the basin. The pluviometric regime is primarily characterized by short-duration and high-intensity rainfall events, mostly occurring in July and August (Gregoretti & Dalla, 2008; Simoni et al., 2020).

Different stony debris-flow events have been recorded in recent decades, probably due to recent changes in the rainfall pattern. The most significant ones occurred on 2 July 1994, 7 August 1996 and 18 July 2009. The first debris flow flooded the inhabited fan with approximately 30 000 m$^3$ of debris. The second mobilized approximately 45 000–60 000 m$^3$ of debris, damaging some houses and cars. The last mobilized approximately 55 000 m$^3$ of debris, and after filling the retaining basin, it flooded the inhabited fan, causing two casualties. The most recent, medium- to high-magnitude debris-flow events occurred on 23 July and 4 August 2015, which mobilized approximately 30 000 and 25 000 m$^3$ of sediments, respectively (for an in-depth analysis, see Simoni et al., 2020).

The proposed research focused on the channel reach encompassed between the initiation area of the Rovina di Cancia debris flow (approximately 1670 m a.s.l) and the human-built depositional area located at approximately 1340 m a.s.l. (excluded). Along this channel section, the Rovina di Cancia debris flow increases in magnitude (i.e. volumetrically grows) since, due to an average bed slope of 25°, it is mainly subject to sediment entrainment processes (Simoni et al., 2020). Therefore, within the study area the modelling of routing should be as reliable as possible, as it provides most of the sediment volume that travels downstream, finally threatening the inhabited areas.

### 2.2 | Terrestrial-based elevation data

The terrestrial-based survey of the Rovina di Cancia study reach was carried out by the research group in October–November 2015 through a dual-frequency Topcon HiPer V GNSS base and rover system capable of tracking both GPS and GLONASS satellite constellations. The survey was carried out as real-time, kinematic, stop-and-go relative positioning based on phase solutions (i.e. rtkGNSS survey) by placing the master station on a known position located within a

maximum distance from the survey area of about 1 km. Furthermore, only fixed solutions were acquired, and the three-dimensional position of each sampled point was calculated as the average of measurements carried out on five epochs. Remarkably, the survey time was chosen according to the best satellite constellation geometry by considering the natural obstacles around the survey area. The instrument-reported planimetric precision was $0.005 \pm 0.001$ m (max. 0.03 m), whereas the reported vertical precision was $0.008 \pm 0.002$ m (max. 0.05 m). The average planimetric dilution of the precision value was $2.55 \pm 0.45$ (max. 3.50). Field sampling was carried out according to a cross-sections, morphologically guided spatial scheme (e.g. Aguilar et al., 2005; Heritage et al., 2009) to describe the channel morphology as accurately as possible. In detail, by following this spatial sampling scheme, higher cross-section and points densities were gathered corresponding to topographically complex channel areas, with comparable lower densities on gentle morphologies. Therefore, the mean points sampling distance was 0.65 m (max. 2.73 m, min. 0.06 m, respectively), whereas the mean cross-sections inter-distance was 3.25 m (max. 9.80 m, min. 0.89 m, respectively). Relevant longitudinal (i.e. toe and top of the channel banks) and transverse (i.e. minor steps) topographic breaklines were also acquired during the field survey. Overall, over 3000 terrestrial-based measurements were collected within the study reach, for an average points density of 1.38 points $m^{-2}$. According to the geodetic–cartographic datum of the aerial-based datasets, the geographic coordinates of the terrestrial-based measurements were projected in the coordinate system WGS84-UTM32, and the orthometric heights were computed by referring to the local geoid model ITALGEO2005 (nominal conversion quality $\pm 0.035$ m at 1$\sigma$).

## 2.3 | Aerial-based elevation data

### 2.3.1 | Helicopter-based full-waveform LiDAR

For the study site at Rovina di Cancia, the LiDAR data were collected on 21 October 2015 by Helica s.r.l. on behalf of the Veneto Region. A full-waveform RIEGL LMS-Q780™ sensor mounted on an I-HBEP helicopter (Eurocopter AS 350B3) flew at approximately 800 m a.g.l. with a scan angle of $\pm 30°$ from nadir by ensuring a side overlap between adjacent flight strips equal to 50%. An onboard GNSS connected via radio waves to five near ground stations (max. distance 50 km) recorded the system carrier position at a frequency of 1 Hz, whereas an IMU rigidly connected to the inner structure of the scanning mechanism sampled the helicopter attitude at a frequency of 200 Hz. Simultaneous aerial photographs were acquired by means of a calibrated Phaseone iXA 180 medium-format frame digital camera with a forward overlap of 65%.

For the study reach, the average raw points density was 20.79 points $m^{-2}$, while the average ground points density was 3.33 points $m^{-2}$. The vertical quality of the laser data was estimated by the vendor through the root mean square error (RMSE) of elevations for 30 ground control points (GCPs) collected within a nearby area. The (stated) RMSE of the elevation value was 0.018 m, with a (stated) mean vertical error of $-0.007$ m.

Since the 'quality' of LiDAR-derived DEMs is strongly affected by classification errors, the delivered datasets were examined before

digital terrain modelling. Notably, the points cloud visual inspection highlighted many data voids within the ground dataset, mainly due to misclassified LiDAR points as overground features corresponding to morphologically complex areas (e.g. bouldered reaches). For this reason, we reclassified the delivered datasets into ground and overground points within the software package LAStools™ (rel. 170 608; Isenburg, 2017) by integrating manual and automatic segmentation procedures. This allowed us to achieve an average ground points density of 4.34 points $m^{-2}$, which is 30% more than the delivered ground dataset density. After the reclassification procedure, the geographic coordinates of the laser-based measurements were projected in the coordinate system WGS84-UTM32, whereas the ellipsoidal heights were converted into the corresponding orthometric heights by referring to the local geoid model ITALGEO2005.

### 2.3.2 | UAV-based SfM digital photogrammetry

For the Rovina di Cancia channel, the UAV imagery was acquired on 6 August 2015 by a private surveyor on behalf of Belluno Province. In detail, a quadcopter equipped with a 12 Mpx RICOH GRX A12 digital camera (equivalent focal length 28 mm) flew at variable heights above the ground level (on average 80 m above each take-off point), gathering a total of 119 images having a ground sampling distance <0.05 m. All photographs were acquired with a nadir orientation of the camera in consecutive single-flight strips by following the stream centreline. Remarkably, despite the near-vertical channel slopes along several sections, no additional terrestrial-based imagery acquisitions were performed.

It is worth noting that the research group was provided only with the acquired imagery in JPG format, without any extra information about the data collection workflow. The SfM-derived points cloud was therefore generated using the Agisoft Photoscan Pro™ software suite (rel. 1.2.6; http://www.agisoft.com). In detail, after a post-processing phase aimed to enhance the quality of the delivered UAV imagery (i.e. local contrast and brightness), the photos were aligned through a high-quality setting in a single chunk. Due to the absence of any other additional information (e.g. camera calibration report), the intrinsic parameters were initialized during the photo's alignment through a self-calibration procedure. Then, they were optimized by means of a bundle adjustment after the filtering of digitally identified matching features, keeping only tie points with a reprojection error and a reconstruction uncertainty lower than 1 and 50, respectively. The dense points cloud was finally obtained through a high-quality setting with an aggressive filtering mode, to sort out most of the outliers. Finally, the SfM-derived points cloud was registered to the coordinate system WGS84-UTM32 through the use of the LiDAR data as reference dataset, similar to what was reported, for example, by Lato et al. (2014). In detail, a seven-parameter similarity transformation was first calibrated by relating homologous 'natural' points (e.g. large boulders) between the RGB-encoded SfM-derived points cloud and 'true' orthorectified LiDAR imagery (pixel size 0.10 m) through an iterative approach by looking for a three-dimensional spatial distribution of the conjugate points as uniform as possible. Due to the potential presence of 'residual' linear errors (e.g. tilts), we then refined the SfM-derived points cloud scaling and spatial roto-translation via a modified version of the iterative closest point algorithm (Besl &

McKay, 1992), which allows for affine transformations (i.e. different scaling along the three axes). Notably, the affine transformation matrix was calibrated by focusing only on densely scanned fully three-dimensional terrain features (e.g. large blocks), located in stable (i.e. unchanged) and possibly low-sloping areas outside the analysed channel reach. Overall, this enabled a 'double' registration process, improving the quality of the SfM-derived points cloud (Cucchiaro et al., 2018) and, simultaneously, the aerial-based datasets co-registration (mean cloud-to-cloud distance 0.03 m). Finally, the linearly transformed SfM-derived points cloud was manually segmented into ground and overground classes to achieve an average ground points density of approximately 180 points m$^{-2}$ (points spacing <0.10 m). All explained points cloud-related operations were performed within the CloudCompare open-source software package (rel. 2.6.1; http://www.cloudcompare.org/).

Since inaccuracies in self-calibrating bundle adjustments could result in systematic errors in the camera orientation estimates as well as in the derived topographic models (e.g. James et al., 2020), prior to data interpolation an extensive vertical quality assessment was carried out on the classified SfM-derived points cloud by using the terrestrial-based measurements as validation data. As a matter of fact, the nominal positioning quality for dual-frequency GNSS receivers operating in real-time kinematic mode with baseline <20 km ranges between 0.02 and 0.05 m, by degrading up to one order of magnitude for both the LiDAR altimetry and the digital photogrammetry also in open-terrain conditions (e.g. Cilloccu et al., 2009; Molina et al., 2014).

In detail, the GNSS dataset was randomly split into two independent and equal-sized samples of more than 1000 measurements (i.e. a training and a validation sub-dataset). The training dataset was employed as reference during the analysis of the vertical 'errors', whereas the validation dataset was used to verify the consistency of the quality estimates. An automated routine based on a proximal point algorithm (e.g. Pourali et al., 2014) was then coded to directly compare the photogrammetric- and terrestrial-derived points coordinates. This approach was deemed the most appropriate for a reliable comparison of topographic measurements, since the inaccuracies introduced through gridding are eliminated (Hodgson & Bresnahan, 2004). Overall, the validation technique involves a user-specified horizontal search radius around the GNSS points for comparison with the SfM-derived points. In order to limit the influence of the channel slope on the computed vertical differences, a horizontal search radius of 0.10 m was chosen after a calibration procedure. This value also allowed an average number of SfM-derived points within the search radii equal to six, ensuring a sufficient sample size for reliable 'error' estimates. All SfM-derived points within that search area were selected, and their orthometric heights were compared to that of the reference GNSS point. The computed elevation differences were considered as vertical 'errors', and they were statistically analysed by using the quality estimators suggested by Höhle and Höhle (2009). The obtained results are summarized in Table S2 in the online Supplementary Material, along with the vertical 'error' estimates of the LiDAR-derived points cloud for comparison. It is noteworthy, for both points clouds, that the systematic component of the vertical error was eliminated through a rigid translation along the z-axis prior to data interpolation.

It should finally be highlighted that during regular field surveys conducted before October–November 2015, we detected only minor changes in the channel morphology compared to August 2015, mainly related to dry ravels from the channel banks that slowly recharge the gully bottom with loose debris. Therefore, in this research, we reasonably assumed that the available topographic datasets described a comparable channel morphology.

## 2.4 | GIS-based cell routing model

The routing modelling of the Rovina di Cancia debris flow was carried out by means of the GIS-based cell routing model proposed by Gregoretti et al. (2019). It represents the fully biphase version of the model proposed by Gregoretti et al. (2016), and notably, it is able to simulate both the routing and entrainment–depositional process of solid–liquid mixtures characterized by a grain collision-dominated rheology (i.e. stony debris flows; Takahashi, 2007).

In summary, the model discretizes the flow domain through the square cells of a raster-grid DEM and routes the solid–liquid flow according to kinematic-wave approximation (e.g. Miller, 1984). Regarding the morphological evolution of the channel bed, the rate of change of bed elevation is calculated through a combination of Exner's equation with a modified version of the empirical one-dimensional law of Egashira and Ashida (1987) by assuming the bottom slope and flow velocity as controlling factors of the erosional–depositional process. Notably, both erosion and deposition are computed only along the steepest downslope flow direction. Finally, from a numerical point of view, the governing equations of the mathematical model are solved by using the finite difference technique, with an explicit scheme subject to the Courant–Friedrichs–Lewy stability condition. A complete description of the employed routing model, along with an illustration of its applicability in real debris-flow events, was reported by Gregoretti et al. (2019).

It is worth mentioning that this model has satisfactorily reproduced (in terms of both erosional and depositional patterns and routing times, if available) three high-magnitude debris flows that occurred in the Dolomites by using nearly the same values of input parameters (Gregoretti et al., 2016, 2018, 2019).

## 3 | METHODS

### 3.1 | Elevation data interpolation

Prior to digital terrain modelling, the overall co-registration of the pre-processed points clouds was assessed through cross-profiling (i.e. extraction of longitudinal and transversal sections) of properly surveyed fully three-dimensional channel features (e.g. large boulders). This allowed the exclusion of any relative linear and/or angular misalignment (i.e. shifts, tilts or scale variations) potentially affecting the research outcomes.

Spatially concurrent DEMs (i.e. orthogonal elevation raster-grids having the same spatial extent) were then generated within the software package ArcGIS™ (rel. 10.6.1; https://www.esri.com/) by first triangulating the pre-processed topographic datasets according to the Delaunay criterion and then converting the obtained triangular irregular networks (TINs) into 1 m-resolution elevation raster-grids through the natural neighbour algorithm (Sibson, 1981). All elevation models were generated with a 1 m cell size, since it was deemed to ensure

the best trade-off among accurate surface representation, data management efficiency and faithful phenomena reproduction. In fact, for the study site, a smaller grid size would not be physically plausible because of the presence at the gully bottom of large sediments (mean diameter up to 1 m) that can be entrained and transported by debris flows. Remarkably, the sampled topographic breaklines were set as constraints during terrestrial-based data triangulation.

The reasons behind the choice of the outlined gridding methodology were threefold. First, the triangular network is a vector-based surface model allowing a better characterization of complex topographic features (e.g. abrupt slope discontinuities) via the inclusion of sampled topographic breaklines as three-dimensional polylines. Second, in the planned gridding methodology, the TIN represents an intermediate model enabling the removal of interpolation artifacts and, through manual editing operations, the improvement of the elevation model 'shape reliability' (here referred to as the degree of maintenance in the model of the gully shape 'complexity'). Finally, according to Boreggio et al. (2018), the triangulation with linear or natural neighbour interpolation, along with the completely regularized spline and thin-plate spline plus tension basis functions, ensures the best trade-off between interpolation quality and 'shape reliability' in a such of morphological environment. Remarkably, the natural neighbour algorithm was in this case preferred over the simplest linear rasterization since it allows a smoother connection among triangle edges by improving the 'shape reliability' of the interpolated surface, mainly in areas featuring low points density values.

## 3.2 | Surface shape analysis

Since the surface shape is the major control over fluxes of water and sediment (e.g. Moore & Grayson, 1991), the performances of each tested survey technology was initially evaluated by exploring the 'shape reliability' of the corresponding DEM (i.e. GNSS-, LiDAR- and UAV-derived DEMs) via digital terrain analysis, as well as cross-profiling in morphologically complex areas (e.g. rugged reaches confined by steep channel banks).

Notably, the digital terrain analysis was carried out based on topographic attributes controlling the routing of gravity-driven flows and related processes (i.e. sediment entrainment and deposition). In detail, we focused on: (1) the terrain slope computed in the direction of steepest descent; (2) terrain roughness (Cavalli & Marchi, 2008); and (3) profile and tangential terrain curvature (Wilson & Gallant, 2000). An automated routine implementing TauDEM™ (rel. 5.3.7; Tarboton, 2003), WhiteBox GAT™ (rel. 1.4.0; Lindsay, 2016) and custom algorithms was coded to compute and analyse all DEMs derivatives.

## 3.3 | DEMs vertical quality analysis

Along with the surface shape analysis, the performances of each tested survey technology were further statistically assessed by characterizing the quality of the derived DEM, under the assumption of a predominantly vertical error. For this task, the terrestrial-based measurements of both the training and validation sub-datasets were used as GCPs.

In detail, for each interpolated DEM, the GNSS points elevation was subtracted from that of the corresponding raster-grid cell centres (i.e. raster-grid cells containing terrestrial-based measurements). For each terrain model, 'elevation residuals' were thus calculated and used to characterize its own vertical error within the R open-source software package (rel. 3.5.0; R Development Core Team, 2008). It must be noted that these 'elevation residuals' were calculated by comparing each time two points datasets, that is, the GNSS points and the corresponding raster-grid cell centres, that did not spatially overlap (points planimetric inter-distance up to 0.71 m). Furthermore, especially in the case of the LiDAR-derived DEM, the compared points datasets also had a different support size. In fact, the LiDAR altimetry collects elevation measurements averaged over the laser beam footprint (i.e. decimetre scale), whereas the GNSS technology provides elevation measurements at the rod tip scale (i.e. centimetre scale). On the other hand, in the case of the GNSS-derived DEM, the compared points datasets were not independent since the elevation model was interpolated by the same points used in the quality assessment. As a consequence of the weaknesses of the outlined procedure, some inherent uncertainties may affect the obtained vertical quality metrics.

Since the derivation of DEM quality measures has to address the presence of outliers and error distributions that may not be normal (Höhle & Höhle, 2009), we followed the approach suggested by Höhle and Potuckova (2011). Basically, this relies on the use of 'standard' (i.e. mean and standard deviation) or robust (i.e. median, normalized median of absolute deviations, NMAD and sample quantiles of the absolute error distribution) quality estimators, depending on whether the vertical error distribution with (or without) outliers is normal. Furthermore, the rule of three times the RMSE was used to set the outlier threshold, while the error distribution normality was tested both graphically and statistically by means of the normal Q–Q plot and the d'Agostino $K^2$ omnibus test, respectively. Notably, the null hypothesis of the test states that the error distribution does not deviate from the normal distribution as a consequence of either data skewness or kurtosis, and the test was chosen due to its power in cases of large samples having kurtosis slightly higher than the normal distribution.

## 3.4 | DEMs vertical uncertainty modelling

As recognized by many authors, the vertical error of DEMs is not spatially uniform and varies according to some spatial pattern (e.g. Erdogan, 2009; Li, 1993; Weng, 2006; Wood, 1996; Wood & Fisher, 1993; Yang & Hodler, 2000). For instance, we may expect higher DEM errors over areas having a low sampled points density and featuring high slope or roughness values (e.g. channel banks) compared to areas having a high sampled points density and a smooth morphology (e.g. debris deposits). However, the quality analysis carried out only provided spatially uniform error estimates (i.e. a unique error value for each elevation model) and, as a result, it did not allow a proper characterization of the inherent vertical error of the interpolated elevation models. Furthermore, the analysis was restricted to raster-grid cells containing surveyed GNSS points, thus not providing comprehensive error estimates. Finally, the survey technologies performances were directly compared through probabilistic DEMs

**TABLE 1** Parametrizations of calibrated FISs

| Parameter | Maximum | Range of values for membership functions | | |
| --- | --- | --- | --- | --- |
| | | Low | Medium | High |
| **GNSS-derived DEM FIS n.3** | | | | |
| Points density (points m$^{-2}$) | 4.00 | 0.00–3.00 | 0.00–4.00 | 2.00–4.00 |
| Euclidean distance to the nearest sampled breakline (m) | 25.96 | 0.00–2.00 | 0.00–4.00 | 2.82–25.96 |
| Terrain slope (°) | 73.71 | 0.00–40.70 | 36.66–48.23 | 44.19–73.71 |
| DEM elevation uncertainty (m) | 0.76 | 0.00–0.25 | 0.03–0.33 | 0.03–0.76 |
| **LiDAR-derived DEM FIS n.3** | | | | |
| Points density (points m$^{-2}$) | 38.00 | 0.00–6.00 | 3.00–9.00 | 6.00–38.00 |
| Euclidean distance to the nearest sampled breakline (m) | 25.96 | 0.00–2.00 | 0.00–4.00 | 2.82–25.96 |
| Terrain slope (°) | 73.71 | 0.00–40.70 | 36.66–48.23 | 44.19–73.71 |
| DEM elevation uncertainty (m) | 1.13 | 0.00–0.31 | 0.03–0.43 | 0.12–1.13 |
| **UAV-derived DEM FIS n.3** | | | | |
| Points density (points m$^{-2}$) | 770.00 | 0.00–188.00 | 169.00–222.00 | 204.00–770.00 |
| Euclidean distance to the nearest sampled breakline (m) | 25.96 | 0.00–2.00 | 0.00–4.00 | 2.82–25.96 |
| Terrain slope (°) | 73.71 | 0.00–40.70 | 36.66–48.23 | 44.19–73.71 |
| DEM elevation uncertainty (m) | 1.64 | 0.00–0.41 | 0.01–0.70 | 0.02–1.64 |

differencing operations. Therefore, since the detectable signal (i.e. differences among compared survey methods) was expected to be of low magnitude, a less conservative and more sophisticated model of the DEMs error was deemed necessary.

To overcome the explained drawbacks, we modelled the DEMs vertical error in a spatially distributed way by using the fuzzy inference system (FIS)-based algorithm proposed by Wheaton et al. (2010). Overall, it allows readily available variables contributing to the DEMs vertical error (e.g. terrain slope or roughness and points density) to be provided as inputs to a FIS, and by relying on a linguistically based rule system, it is able to output spatially variable estimates of the DEMs elevation uncertainty (or 'error'). For a complete dissertation on the algorithm and its applicability, the reader is referred to Wheaton (2008) and Wheaton et al. (2010).

In this research, we developed ad hoc FISs for GNSS-, LiDAR- and UAV-derived DEMs. In detail, for each FIS, we used three input variables, namely: (1) points density (a surrogate of the topographic measurement spatial arrangement); (2) Euclidean distance to the nearest sampled topographic breakline (a surrogate of the error clustering); and (3) terrain slope (a surrogate of the topographic complexity). These spatial indicators of elevation uncertainty were chosen by previously investigating their relationships with the computed elevation 'errors' by means of a bivariate correlation analysis. As pointed out by Hensleigh (2014), this represents a key preliminary step since the real work in developing a FIS consists of recognizing the variables actually affecting the DEM error and exploring their mutual relationships. Notably, for all FISs, each input variable was classified into three fuzzy sets (i.e. low, medium and high), whose value ranges were defined by analysing the sample distribution and corresponding quantiles.

Once both the input variables and corresponding fuzzy sets were defined, linguistically-based FIS rule systems relating inputs to output (i.e. DEMs elevation uncertainty) were set up, and then the value ranges of the three fuzzy sets (i.e. low, medium and high) of the output variable were calibrated based on the observed DEMs errors.

Finally, for each possible combination of input variables, the corresponding output fuzzy set was identified.

It is worth highlighting that for each interpolated elevation model, we parametrized three separate FISs (for a total of nine independent FISs) in a sort of calibration procedure by changing the fuzzy set value ranges of both input and output variables (Table 1). Each developed FIS was then validated by comparing the modelled and observed DEM errors and their corresponding distributions. The geomorphic change detection (GCD) ArcGIS™ plugin (rel. 6.1.14; http://gcd. riverscapes.xyz/) was used to implement all FISs.

## 3.5 | Survey technologies comparison

In this study, the differences among tested survey technologies were estimated at the raster-grid cell scale by subtracting the corresponding DEMs values (e.g. GNSS-derived DEM vs. LiDAR-derived DEM). As a result, three independent DEM of difference (DoD) raster-grids (i.e. DoD$_{GNSS-LiDAR}$, DoD$_{GNSS-UAV}$ and DoD$_{LiDAR-UAV}$), showing in a spatially distributed way the magnitude of the vertical discrepancies between compared survey technologies were obtained.

As stressed by different authors, in attempting DEMs subtraction exercises, it is essential to properly account for the inherent uncertainties of the differenced surfaces to distinguish any detectable signal from the background noise (e.g. Bangen et al., 2014; Lane et al., 2003; Milan et al., 2011; Passalacqua et al., 2015; Schaffrath et al., 2015; Wheaton et al., 2010). Most DEMs differencing analyses rely on the 'standard' error propagation (Taylor, 1997) and some form of thresholding, thus resulting in a definition of a minimum level of detection ($_{min}$LoD) above which the calculated vertical differences between compared surfaces are assumed to be significant. In this context, the most recent and advanced approach consists of a probabilistic thresholding of the DoD raster-grid at any chosen confidence interval (CI; e.g. 68, 95 or 99%) by using spatially variable DEMs error

estimates (e.g. FISs-based DEMs uncertainty estimates). Therefore, a unique $_{min}$LoD is calculated on a cell-by-cell basis by multiplying the propagated DEMs error by a critical Student's $t$-value (e.g. 1.96 for a 95% CI), on the assumption that the individual DEMs errors are independent and distributed according to a Gaussian function.

In this research, to recognize the magnitude and spatial distribution of the significant discrepancies among compared survey technologies, we thresholded the three derived DoD raster-grids at a 95% probabilistic CI by using the corresponding spatially variable FIS-based DEMs error estimates. Remarkably, both a 68.3% and a 99% probabilistic CI was used further to test the influence of the chosen critical Student's $t$-value on the obtained results.

## 3.6 | Evaluation of the topographic data source effect on debris-flow routing modelling

Since an inaccurate model parametrization could hide the topographic data source effect on routing modelling, we remark that the employed model parameter values were those that allowed the close reproduction of three debris-flow events that occurred in the Dolomites, including the one that affected the study area of Rovina di Cancia in July 2009 (approximately 55 000 m³ of entrained and transported sediments). Moreover, a sensitivity analysis carried out by Gregoretti et al. (2019), relying on the data of the July 2009 debris-flow event, highlighted that variations in the model parameters values within a physically plausible range did not lead to significantly different routing-modelling outcomes. Overall, this should ensure a reliable analysis of the topographic data source effect on debris-flow routing modelling.

In all performed model runs, the values of the model parameters along with the upstream boundary condition (i.e. inlet solid–liquid discharge hydrograph of assigned return period) were kept unchanged, thus varying only the initial topographic surface where the flow occurs. Therefore, this exercise allowed the investigation of the inherent impact of the employed survey technology on the routing model behaviour.

In this research, two event scenarios (i.e. 300- and 50-years return period) were defined and used in the different model runs, thus evaluating the influence of the topographic data source in two different flow conditions, characteristics of two usual design return periods. Therefore, a total of six model runs were executed (i.e. three initial topographic surfaces times two event scenarios).

To assess the topographic data source effect on debris-flow routing modelling, the model runs outcomes comparison was carried out by focusing on those concerning the hazard, namely: (1) the solid–liquid discharge hydrographs corresponding to five control cross-sections; (2) the areas inundated during propagation; (3) the erosional–depositional volumes; and (4) the erosional–depositional depths, maximum flow depths and maximum thicknesses corresponding to thirty-eight, 2 m-buffered cross-sections evenly distributed within the computational domain (cross-sections inter-distance <20 m). With regard to the last analysis, both a 0.50 m and a 1 m buffer were used to assess the impact on the obtained results.

It is worth highlighting that ground reference informations for both modelled event scenarios were not available. Therefore, the investigation must be considered a sensitivity study rather than a quality assessment, answering the following research question: How may we expect the routing model behaviour to differ if we use as input bathymetry DEMs generated by gridding topographic datasets of different source?

## 4 | RESULTS AND DISCUSSION

### 4.1 | Surface shape analysis

The results of the 'shape reliability' analysis of generated elevation models globally highlight a change in the shape 'complexity' of the reproduced gully morphology, depending on the topographic data source (Figure 2 and Figure S1 in the online Supplementary Material).

For each terrain attribute considered, the comparative analysis of the corresponding raster-grid box plots (Figure 2) points out noticeable differences, mainly in terms of value dispersion (i.e. interquartile range and distribution extremes). In detail, the GNSS-based DEM derivatives feature the lowest data dispersion ($41.22 \pm 9.22°$, $0.01 \pm 0.02$ m, $0.31 \pm 4.46°$/m and $0.84 \pm 6.96°$/m for the terrain slope, roughness, profile and tangential curvature, respectively), thus denoting a poorly detailed and generally smooth interpolated surface, mostly due to the inherent limits of the survey technology (i.e. low density and non-uniform spatial arrangement of the sampled points). Conversely, for the same terrain attributes, the highest raster-grid data dispersion is observed in the UAV-based DEM derivatives ($41.98 \pm 11.60°$, $0.03 \pm 0.07$ m, $0.33 \pm 7.40°$/m, and $0.78 \pm 13.77°$/m, respectively), probably due to the extremely high topographic data source resolution (up to 500 ground points m$^{-2}$), allowing the digital modelling of more 'complex' shapes (e.g. boulders, near-vertical slopes, loose debris deposits and scour limits). On the other hand, the aerial-based full-waveform laser altimetry yielded a digital representation of the gully surface with in-between shape 'complexity' ($41.74 \pm 10.60°$, $0.02 \pm 0.05$ m, $0.38 \pm 6.21°$/m and $0.95 \pm 11.33°$/m for the terrain slope, roughness, profile and tangential curvature, respectively), likely due to the use of a full-waveform sensor (and related data post-processing algorithms) ensuring both a density (up to 20 ground points m$^{-2}$) and a spatial arrangement of the topographic measurements suitable to adequately resolve the channel singularities.

The outlined differences in the modelled surfaces 'complexity' are also underpinned by the visual assessment of Figure S1 cross-profiles and 3D views. In fact, it clearly stresses the inability of the terrestrial measurements-based DEM to properly reproduce both complex channel bottom forms (e.g. rock step and boulders) and gully banks, since they were not fittingly surveyed, mostly due to site accessibility-related safety reasons. On the other hand, mostly due to the higher density and more uniform spatial distribution of sampled points, the aerial-based survey technologies yielded a more faithful and finer representation of the terrain features affecting the gravity-driven flow dynamics (e.g. channel banks, steps and rugged areas), thus guaranteeing a higher 'shape reliability' of the corresponding elevation models.
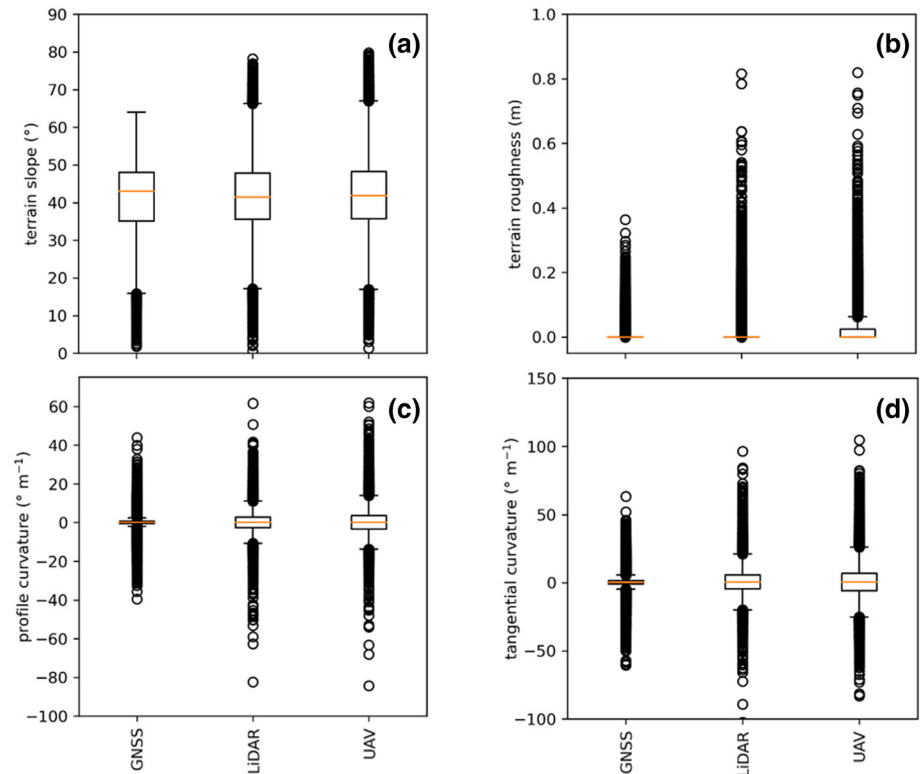
**T A B L E 2**   Computed standard and robust DEMs quality statistics

|  | GNSS-derived DEM | LiDAR-derived DEM | UAV-derived DEM |
|---|---|---|---|
| Number of outliers ($-$) | 30.00 | 50.00 | 35.00 |
| Mean (m) | 0.00 | $-0.06$ | $-0.09$ |
| Standard deviation (m) | 0.25 | 0.38 | 0.62 |
| Mean after the outliers thresholding (m) | 0.00 | $-0.05$ | $-0.10$ |
| Standard deviation after the outliers thresholding (m) | 0.24 | 0.34 | 0.57 |
| Median (m) | 0.00 | $-0.03$ | $-0.04$ |
| NMAD (m) | 0.22 | 0.30 | 0.41 |
| 68.3% quantile of absolute errors (m) | 0.23 | 0.31 | 0.47 |
| 95% quantile of absolute errors (m) | 0.52 | 0.79 | 1.41 |

## 4.2  |  DEMs vertical quality analysis

The GNSS-, LiDAR- and UAV-derived DEMs vertical quality metrics, computed by comparing the terrestrial-based elevations to those of the corresponding raster-grid cell centres, are summarized in Table 2. For the GNSS-derived DEM, the values of the 'standard' quality estimators (i.e. mean and standard deviation) computed on the error sample after outlier thresholding do not differ significantly from those of the robust estimators (i.e. median and NMAD). Conversely, the outliers have a great influence on the computed mean and standard deviation values for both LiDAR- and UAV-derived DEMs. In fact, after outlier thresholding, their values decrease by remaining greater than the corresponding robust ones. Therefore, in this research, the median and NMAD were used to characterize the quality of all interpolated elevation models. Furthermore, the 95% quantile of the absolute error distribution was employed as a robust estimator of the maximum (unsigned) vertical error.

Overall, the median of the vertical errors can be regarded as negligible for all gridded surfaces, indicating that the three investigated survey methods are not biased (i.e. they do not systematically over- or under-estimate elevation values). The median of the vertical errors for the LiDAR- and UAV-derived DEMs is only slightly biased towards under-estimating elevation values ($-0.03$ and $-0.04$ m, respectively). Notably, this vertical bias was eliminated before undertaking the DEMs differencing exercise by means of a rigid translation in the z dimension of both surfaces.

By looking at the quality metrics, the error estimates are 'better' for the GNSS-derived DEM (NMAD 0.22 m) with respect to both LiDAR- and UAV-derived DEMs (NMAD 0.29 and 0.41 m, respectively). However, this may depend on the use of terrestrial-based measurements as reference values in the performed vertical quality assessment. Overall, the quality estimates are smaller than 0.30 m for both GNSS- and LiDAR-derived DEMs. Conversely, for the UAV-derived DEM, the NMAD of the computed elevation errors is >0.40 m, thus denoting a vertical quality lower than the one obtained by the research group for SfM-derived DEMs related to debris-flow channels of the test area of Fiames (Cortina d'Ampezzo, north-eastern Italian Alps). Therefore, since the low determinability of the camera's

additional parameters (e.g. radial distorsion parameters) in self-calibrating bundle adjustments of relatively weak imaging configurations, combined with possible correlations between intrinsic and extrinsic photogrammetric parameters, could impair the quality of derived topographic models (e.g. James & Robson, 2012; James et al., 2020; Wackrow & Chandler, 2008, 2011), we characterized the radial variation of the vertical error (see Figure S2 in the online Supplementary Material) as well as the magnitude of the doming deformation of the SfM-derived points cloud, as described by James and Robson (2014) and James et al. (2020). Overall, from the analysis of the trend of the scatter plots shown in Figure S2, it is reasonable to suppose that the followed workflow, as well as the high topographic gradien and morphological complexity of the study reach (average slope 25°), combined with the variability in both the flight altitude and camera pointing directions, allowed us to effectively counteract the quality issues related to the weak imaging configuration (dome amplitude <0.01 m). However, a closer look at the plots reveals a complex spatial pattern of the vertical error. On the one hand, as previously observed by James et al. (2020), this appears to suggest that, although

the magnitude of the SfM-derived points cloud deformation is not statistically significant (p-value > 0.1), the spatial distribution of the error is more complex and difficult to compensate, likely due to the strong topographic relief of the study site. On the other hand, in agreement with the quality-based classification of DEMs proposed by Cilloccu et al. (2009), this highlights that only GNSS and full-waveform laser altimetry technologies were able to provide dense (i.e. high-resolution) and high-quality DEMs of the study area, ideally suitable for flow-routing modelling applications. However, the 'shape reliability' analysis of generated elevation models clearly highlighted the inability of the terrestrial measurements-based DEM to properly reproduce the terrain features affecting gravity-driven flow dynamics (e.g. channel banks, steps and rugged areas; Figure S1), mostly due to the inherent limits of the survey technology. In contrast, the photogrammetric-based survey technology proved to ensure a more faithful and detailed representation of gully morphology, with the highest observed shape 'complexity', likely due to the extremely high topographic data source resolution (Figures 2 and S1). This evidence emphasizes the primary role of shape analysis techniques (also in the
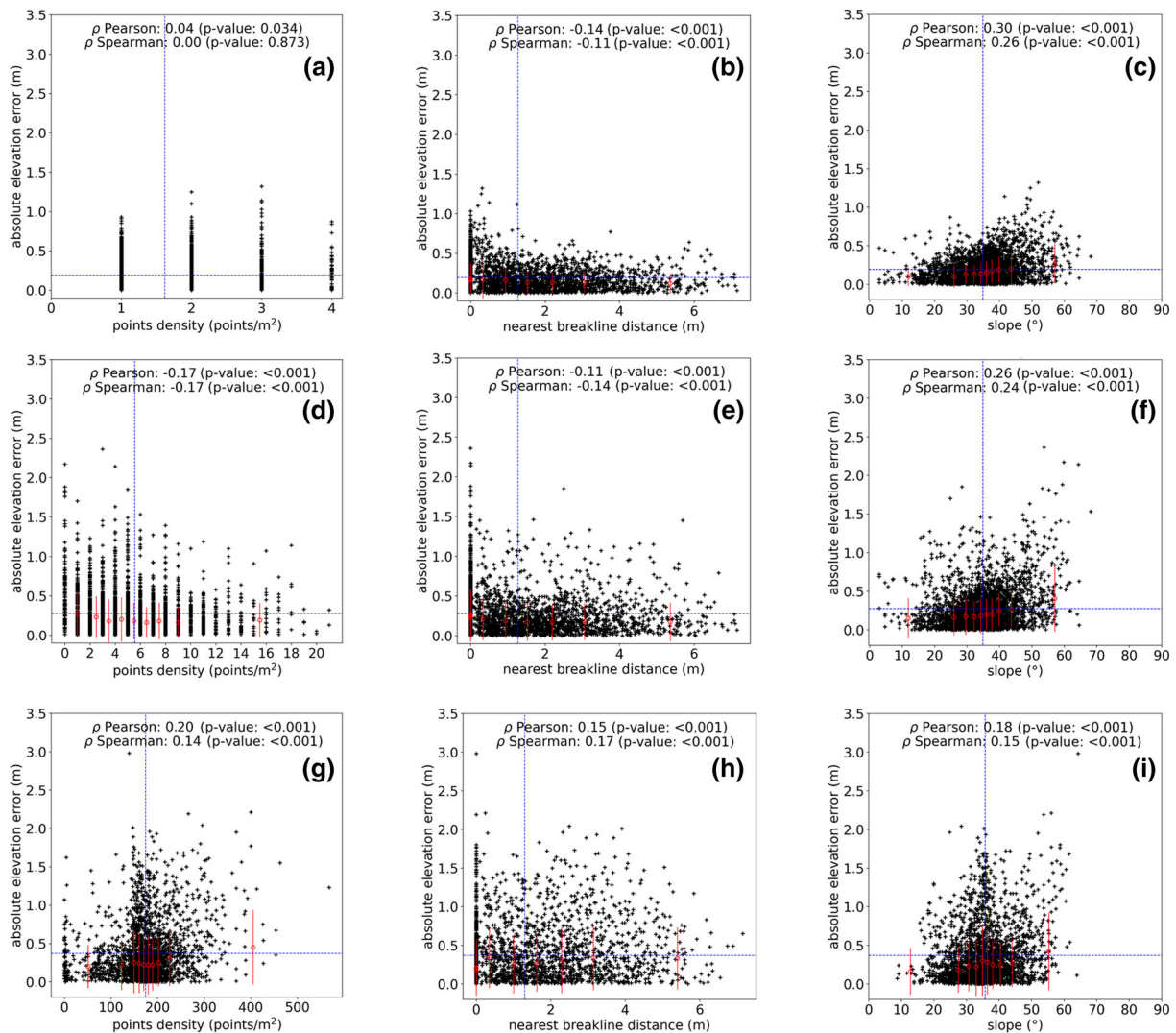


**FIGURE 3** Scatter plots of the points density (a, d and g), Euclidean distance to the nearest sampled topographic breakline (b, e and h) and terrain slope (c, f and i) values against the observed absolute errors of GNSS- (top), LiDAR- (centre) and UAV-derived (bottom) DEMs. For elucidating global trends, both the median and NMAD of the absolute elevation errors for each decile of the input FISs variables are also depicted (red circles and corresponding whiskers, respectively). *Note*: The dotted blue lines represent the marginal means of correlated variables
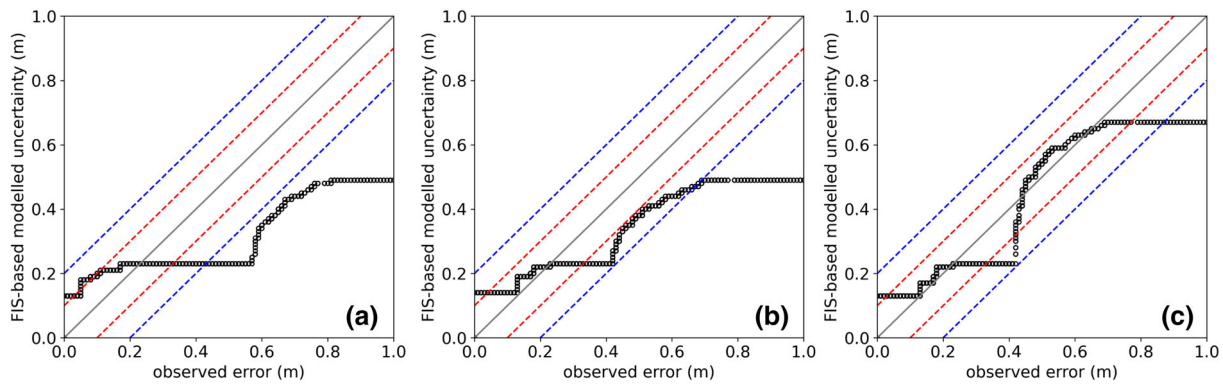
**FIGURE 4** Q–Q plots relating the observed and modelled elevation errors for the LiDAR-derived DEM: (a) FIS n.1, (b) FIS n.2 and (c) FIS n.3. *Note*: The continuous grey line depicts the 1:1 relationship, whereas the blue and red dashed lines correspond to a FIS error of ±0.10 and ±0.20 m, respectively
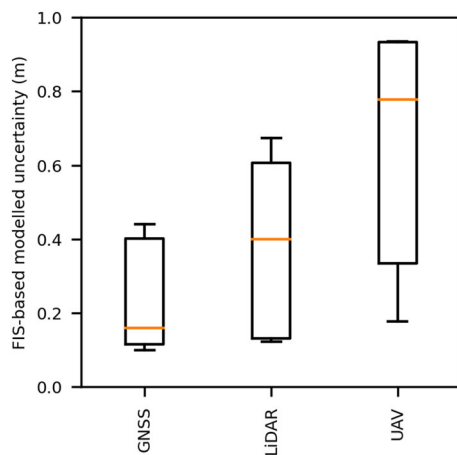


**FIGURE 5** Box plots summarizing the modelled FIS n.3-based elevation uncertainty for each interpolated DEM

simplest form of cross-profiling) when undertaking DEMs-related analyses, as they effectively compensate for the inherent limits of the purely statistics-based approach.

## 4.3 | DEMs vertical uncertainty modelling

In Figure 3 (top and centre), we report the results of the bivariate correlation analysis between the three chosen FIS input variables (i.e. points density, Euclidean distance to the nearest sampled topographic breakline and terrain slope) and observed absolute errors of GNSS- and LiDAR-derived DEMs. As expected, the global trends highlight a positive correlation between the channel bottom slope and observed absolute errors and a negative correlation between the points density and Euclidean distance to the nearest sampled topographic breakline. First, this indicates that the DEMs error generally tends to be higher corresponding to both high-gradient areas featuring a low sample points density and at slope discontinuities, in agreement with what has been observed by many previous authors (e.g. Boreggio et al., 2018; Erdogan, 2009; Heritage et al., 2009; Milan et al., 2011; Scheidl et al., 2008; Wheaton et al., 2010). Second, this also indicates that the chosen spatial indicators of elevation uncertainty are suitable proxies for factors contributing to the DEMs

vertical error, which can in turn be used as input variables in a FISs-based DEMs error model. Notably, all plots show a points pattern having a progressive dispersion (i.e. a megaphone pattern), hence indicating that low-magnitude elevation uncertainties can also be observed at both high-gradient areas having a low sample points density and at slope discontinuities. In fact, although these conditions increase the potential for higher DEMs uncertainties, accurate DEMs elevation values are still possible.

In Figure 3 (bottom), we report the results of the bivariate correlation analysis carried out for the UAV-derived DEM. Notably, the global trends point out a positive correlation for both the points density and Euclidean distance to the nearest sampled topographic breakline, in contrast to what was explained previously. Overall, this indicates that the UAV-derived DEM errors tend to be higher corresponding to high-gradient areas located far from the channel banks (i.e. sampled major topographic discontinuities) and featuring high points density values. On the one hand, the positive correlation for the points density may be due to a significant increase in the local variance (i.e. of the high-frequency component) of the SfM-derived points cloud (and of the corresponding TIN) with the sample points density, as a consequence of either a rise of the instrument-related noise or a more detailed description of the submetre-scale channel topography (or a combination of them). In the latter case, this in turn results in more inaccurate error estimates, mostly due to the extremely local character of the triangulation process in the high points density condition and the spatial mis-overlap between the GCPs used and corresponding raster-grid cell centres. On the other hand, the positive correlation for the Euclidean distance to the nearest sampled topographic breakline may be related to the 'natural' increase in the terrain roughness by moving from the channel banks to the talweg because of the loose debris deposits, which in turn yields a significant increase in the local variance of the SfM-derived points cloud with more inaccurate error estimates. To investigate this thesis, the SfM-derived points cloud was also gridded by averaging (1 m support size), thus reducing the influence of: (1) the high-frequency component; (2) the inherent limits of the error assessment methodology; and (3) the points density on the interpolation process. As depicted in Figure S3 in the online Supplementary Material, the global trends of the average-derived DEM also highlight a positive correlation for both variables, thus rejecting the postulated hypotheses. As previously pointed out, the presence of a complex spatial
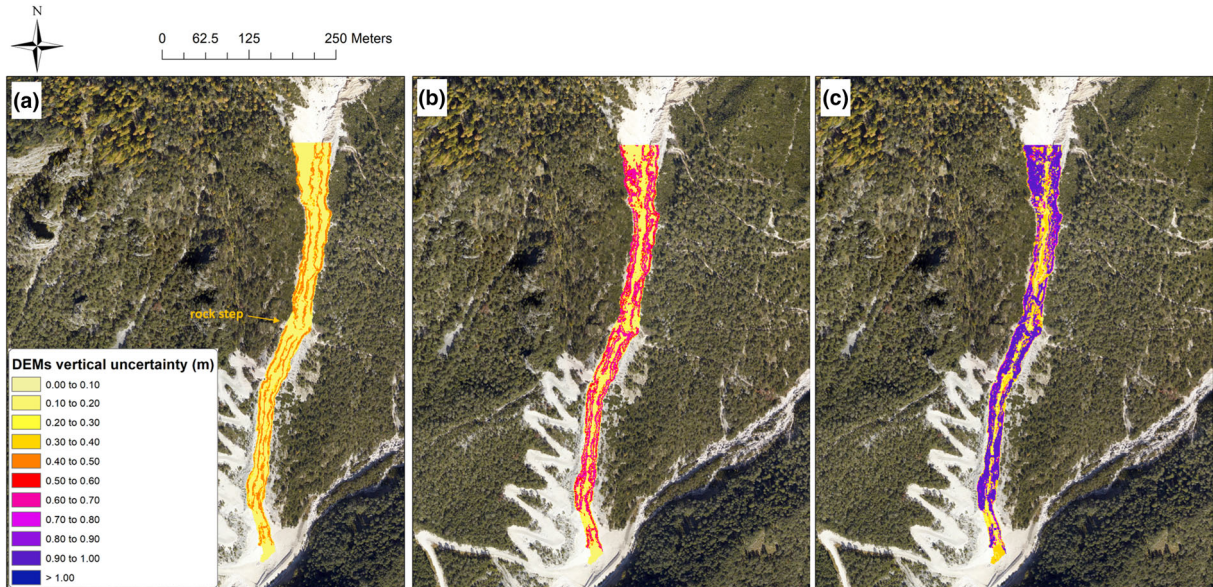
**FIGURE 6**    FIS n.3-based elevation uncertainty raster-grids for (a) GNSS-, (b) LiDAR- and (c) UAV-derived DEMs
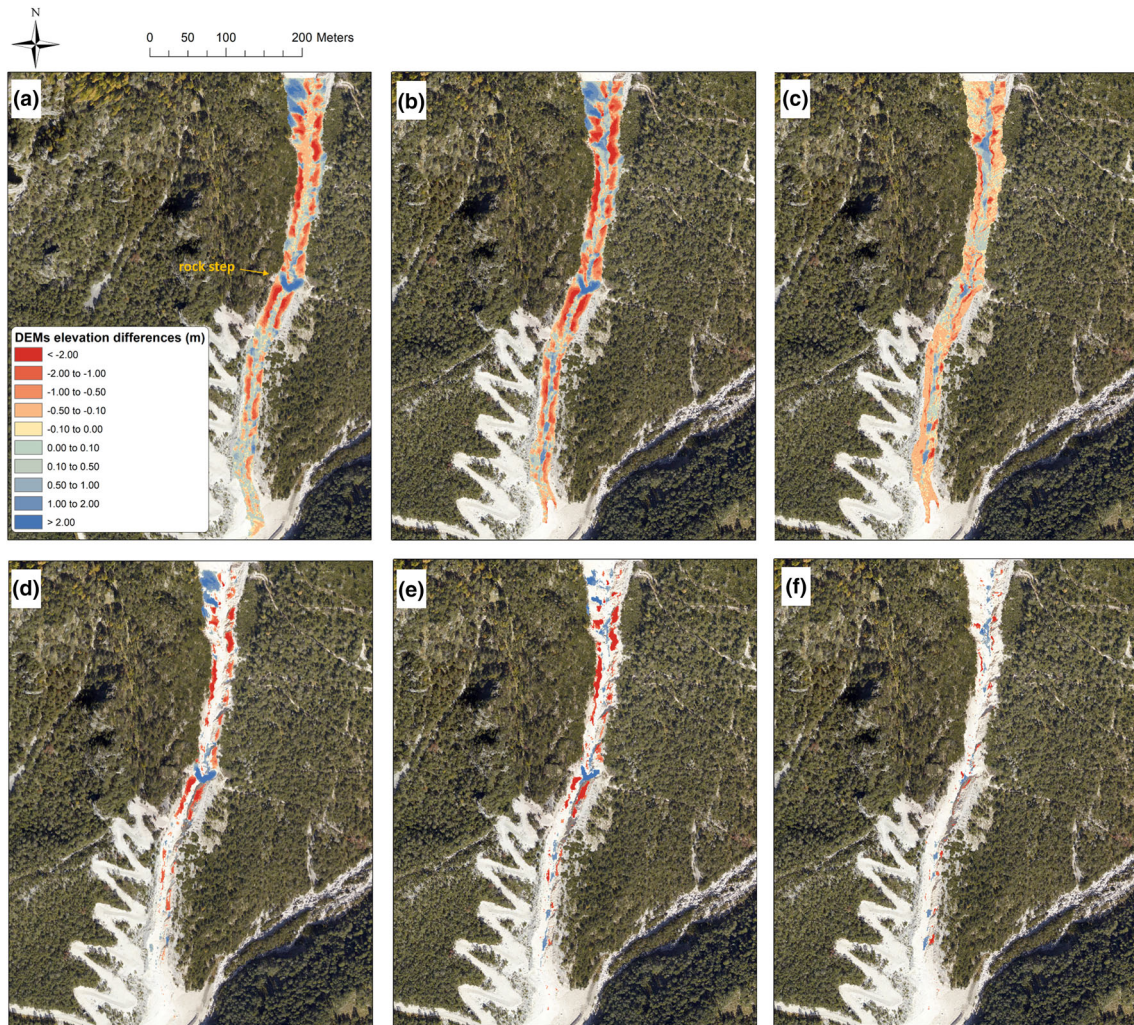


**FIGURE 7**    Unthresholded (a, b and c) and corresponding thresholded (95% CI; d, e and f) DoD raster-grids, calculated using the propagated FISs-based DEMs elevation uncertainty estimates (Figure 6). Left (a and d): GNSS- and LiDAR-derived DEMs comparison; centre (b and e): GNSS- and UAV-derived DEMs comparison; and right (c and f): LiDAR- and UAV-derived DEMs comparison

**FIGURE 8** Simulated solid–liquid discharge hydrographs for 300-years return period model runs corresponding to GNSS-, LiDAR- and UAV-derived DEMs (blue, red and green, respectively)
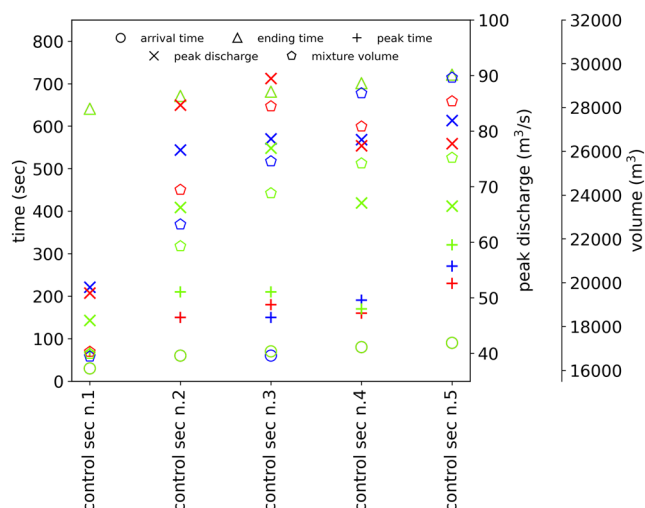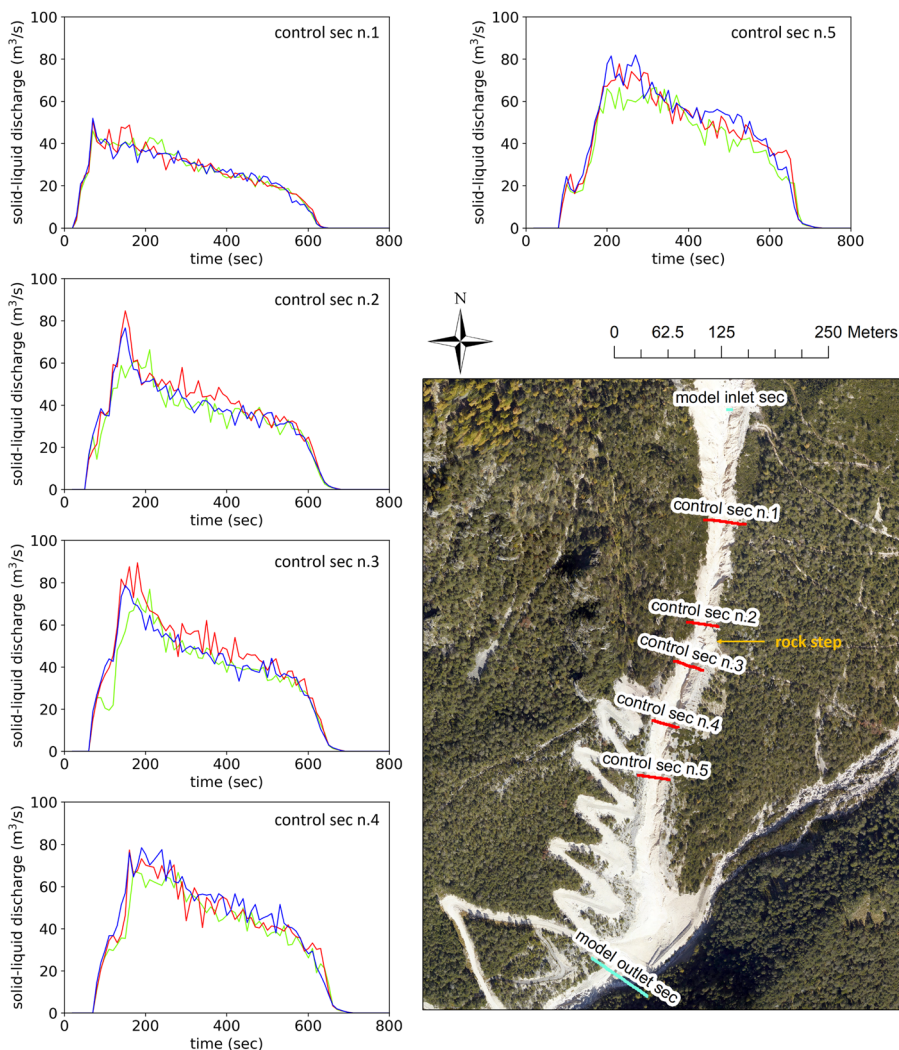




**FIGURE 9** Characteristic times and peak discharges of simulated 300-years return period solid–liquid discharge hydrographs. *Note*: Blue, red and green colours represent the model runs corresponding to GNSS-, LiDAR- and UAV-derived DEMs, respectively

pattern of vertical errors may explain the conflicting trends observed in this study. Therefore, to confirm these findings, further investigations on other SfM-derived datasets related to debris-flow channels are currently underway in the test area of Fiames.

Notably, the investigation of Figure 3 plots indicates that at the sampled major topographic discontinuities (i.e. toe and top of the channel banks), the GNSS-derived DEM features the lowest absolute error values. Overall, this suggests that despite the recognized global poor shape 'reliability' (see Figure S1), the terrestrial measurements-based DEM is able to model sharp slope changes more accurately than the aerial measurements-based DEMs, likely due to the setting of the sampled topographic breaklines as constraints during the triangulation process. As a consequence, this allows the gridding algorithm to reliably model sharp edges, even in the case of topographic datasets with quite low points density. On the other hand, for this kind of morphological environment, it is also stressing the significance of an interpolation algorithm allowing the inclusion of sampled topographic breaklines as constraints, even in the case of high points density topographic datasets (e.g. SfM-derived points clouds). However, it is worth noting how the comparison of the absolute errors of the LiDAR- and UAV-derived DEMs at abrupt slope changes indicates that even without the use of sampled breaklines, a higher sample points density ensures a more reliable sharp edge modelling (with this kind of gridding methodology).

As an example, the Q–Q plots in Figure 4 summarize the relationship between the observed and modelled LiDAR-derived DEM errors for its three developed FISs (see Table 1). Overall, for each interpolated DEM, the best agreement is achieved by FIS n.3, with the closest 1:1 relationship between the observed and modelled DEMs errors.

Remarkably, a closer look at the plots reveals that all FISs-based DEMs error models yield a loss of the observed error variance by under-estimating the largest observed DEMs error values and by over-estimating the smallest ones. As pointed out by Hensleigh (2014), this may be due to the inability of the FISs-based DEMs error models to account for situations where the elevation error can be both of high and low magnitude at the same time, thus not replicating the observed megaphone pattern (Figure 3). Furthermore, the DEMs error is truly a complex function of the points 'quality', sampling density, morphological complexity, gridding methodology and raster-grid spatial resolution. Therefore, it is unlikely that the implemented (three-input variables) FISs can provide a comprehensive characterization of the error of interpolated DEMs.

Overall, the FIS n.3-based DEMs elevation uncertainty estimates are in the range 0.10–0.44, 0.12–0.67 and 0.18–0.93 m for the GNSS-, LiDAR- and UAV-derived DEMs, respectively. Furthermore, as shown in Figure 5, the uncertainty estimates are lower (median 0.16 m) and have a smaller variance (standard deviation 0.13 m) in the

case of the GNSS-derived DEM relative to both the LiDAR- and UAV-derived DEMs (median 0.40 and 0.77 m, standard deviation 0.22 and 0.31 m, respectively). However, it must be stressed that the fuzzy set value ranges of the FISs output variable (i.e. modelled DEMs elevation uncertainty) were calibrated based on the elevation errors computed through the use of terrestrial-based measurements as GCPs. Remarkably, of the three interpolated DEMs, the UAV-derived DEM has the highest modelled inherent uncertainty (Figures 5 and 6).

As shown in Figure 6, the FIS n.3-based elevation uncertainty estimates are generally higher at the major longitudinal (i.e. toe and top of the channel banks) and transverse (i.e. massive rock step located at the end of the triggering reach; Figure 1) topographic discontinuities and along the channel banks, especially for the UAV-derived DEM. Conversely, the lowest-magnitude uncertainty estimates are observed along the channel bottom. Overall, this indicates that all investigated survey technologies are able to describe the area mainly affected by the routing of channelized debris flows with a generally lower inherent noise and comparable higher uncertainty values
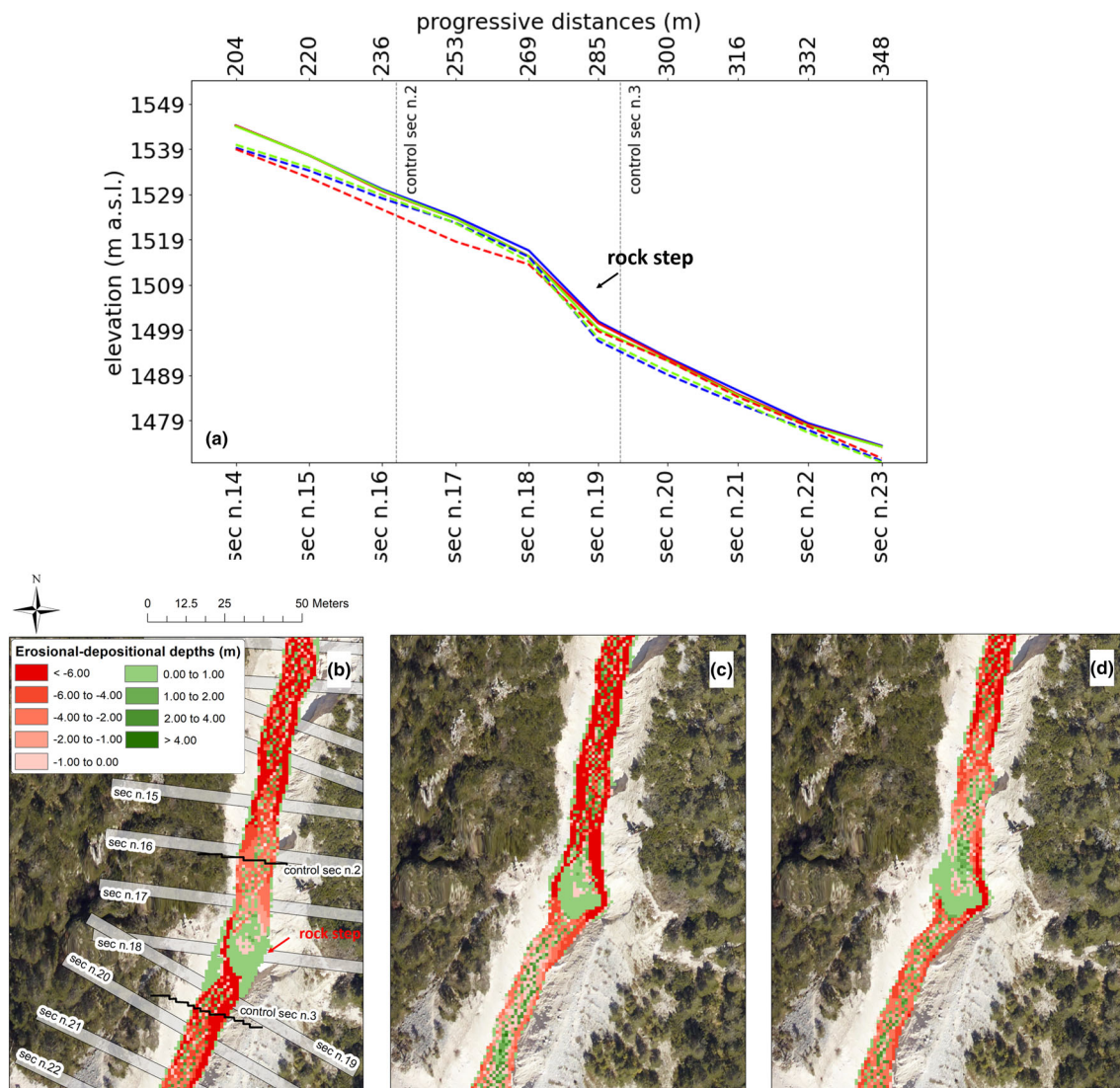


**FIGURE 10** (a) Terrain profiles before (continuous lines) and after (dashed lines) the modelled 300-years return period event scenario, with a focus on the massive rock step located about 300 m downstream the inlet section (*note*: blue, red and green colours represent the model runs corresponding to GNSS-, LiDAR- and UAV-derived DEMs, respectively). *Note*: The profiles show the mean terrain elevation of the inundated area during the propagation, computed corresponding to the depicted 2 m-buffered inner domain cross-sections. Bottom: Simulated erosional–depositional depths at the end of 300-years return period model runs: (b) GNSS-, (c) LiDAR- and (d) UAV-derived DEMs

corresponding to morphologically complex transverse and longitudinal terrain features.

## 4.4 | Survey technologies comparison

The unthresholded DoD raster-grids, along with the corresponding probabilistically thresholded models (95% CI) are shown in Figure 7.

For the GNSS- and LiDAR-derived DEMs comparison (Figures 7a and D), the computed vertical discrepancies range from −4.31 to 6.39 m, with an average (thresholded) vertical difference of −0.07 m. Therefore, the LiDAR-derived DEM is slightly biased towards over-estimating the GNSS-derived DEM elevations. The visual assessment of the unthresholded DoD map (Figure 7a) reveals that most computed elevation discrepancies feature a low magnitude, indicating an overall fair agreement between the two compared survey technologies. Furthermore, as shown in the corresponding thresholded DoDs raster-grid (Figure 7d), most computed vertical differences are not significant when probabilistically thresholded at a 95% CI (total volumetric unthresholded and thresholded difference between compared DEMs of 11709.82 and 7212.26 m³, respectively). Statistically significant elevation discrepancies are observed along the channel banks and corresponding to the massive rock step, where no terrestrial-based measurements were gathered in the field due to site accessibility-related safety reasons. Conversely, along the channel bottom, no meaningful vertical discrepancies are detected. Overall, this indicates that a low-altitude, helicopter-based, full-waveform LiDAR survey has the potential to provide a topographic characterization of the bathymetry of a debris-flow channel comparable (i.e. not significantly different) to that of a cross-sections, morphologically guided terrestrial-based geodetic survey. On the other hand, a GNSS survey cannot ensure a reliable characterization of complex channel bottom forms (e.g. rock steps and bouldered reaches; Figure S1) and longitudinal features (e.g. high-gradient channel banks; Figure S1) if they are not properly surveyed in the field.

Regarding the GNSS- and UAV-derived DEMs comparison (Figures 7b and e), the computed vertical discrepancies range from −4.73 to 6.76 m, with an average (thresholded) vertical difference of −0.13 m. Therefore, the UAV-derived DEM is biased towards over-estimating the GNSS-derived DEM elevations to a greater extent than the LiDAR-derived DEM (total volumetric unthresholded and thresholded differences 14 708.98 and 7428.52 m³, respectively). The visual assessment of the corresponding DoD raster-grids indicates that (also for this comparison) the statistically significant elevation discrepancies are mainly concentrated along the channel banks and corresponding to the massive rock step due to the remarked inherent limits of the terrestrial-based survey technology. Conversely, along the channel bottom, no meaningful vertical discrepancies are detected overall, except for minor patches mainly related to bouldered channel reaches and, to a minor extent, the manual removal of uprooted shrubs within the SfM-derived points cloud. However, it should be observed that the (cell-scale) DoD raster-grid thresholds are generally higher than those referred to in the GNSS- and LiDAR-derived DEMs comparison due to the higher inherent uncertainty of the UAV-derived DEM (Figures 5 and 6). This may explain the general absence of significant elevation discrepancies between the two compared survey technologies along the channel bottom, despite the
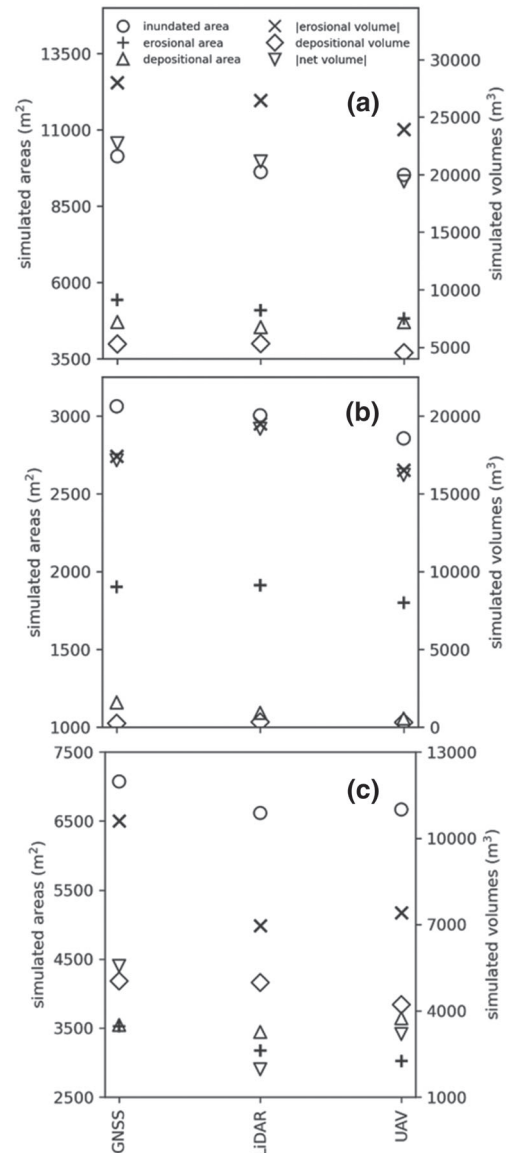


**FIGURE 11** Three hundred years return period model run results in terms of simulated inundated areas and erosional–depositional volumes at the (a) domain, (b) upstream and (c) downstream the rock step-scale

recognized meaningful differences in the 'complexity' of the reproduced surface (Figures 2 and S1).

Finally, in the case of the LiDAR- and UAV-derived DEMs comparison (Figures 7c and f), the computed vertical discrepancies range from −3.65 to 2.51 m, with an average (thresholded) vertical difference of −0.15 m. Therefore, the UAV-derived DEM is also biased towards over-estimating the LiDAR-derived DEM elevations. A visual assessment of the unthresholded DoD model (Figure 7c) indicates that the computed elevation discrepancies generally feature a low magnitude along both the channel bottom and channel banks, hence indicating a fair agreement also between these two survey technologies. Some minor patches of high-magnitude discrepancies are especially observed within the areas affected by manual editing operations (i.e. uprooted vegetation removal) of the SfM-derived points cloud. Furthermore, as shown in the corresponding thresholded DoD model (Figure 7f), most computed vertical discrepancies are not significant when probabilistically thresholded at a 95% CI (total volumetric

unthresholded and thresholded differences 6531.23 and 1979.09 m³, respectively). Notably, minor patches of significant elevation discrepancies between compared DEMs are recovered corresponding to abrupt slope discontinuities by thresholding the DoD raster-grid in Figure 7c at a CI of 68.3%, mainly due to the ability of SfM-based digital photogrammetry to faithfully model 'complex' shapes (e.g. near-vertical slopes and scour limits; Figures 3 and S1).

## 4.5 | Evaluation of the topographic data source effect on debris-flow routing modelling

Figures 8 and 9, along with Figures S4 and S5 in the online Supplementary Material, show the model runs results in terms of solid–liquid discharge hydrographs simulated at the five depicted control cross-sections, as well as the corresponding volumes, 'characteristic times'
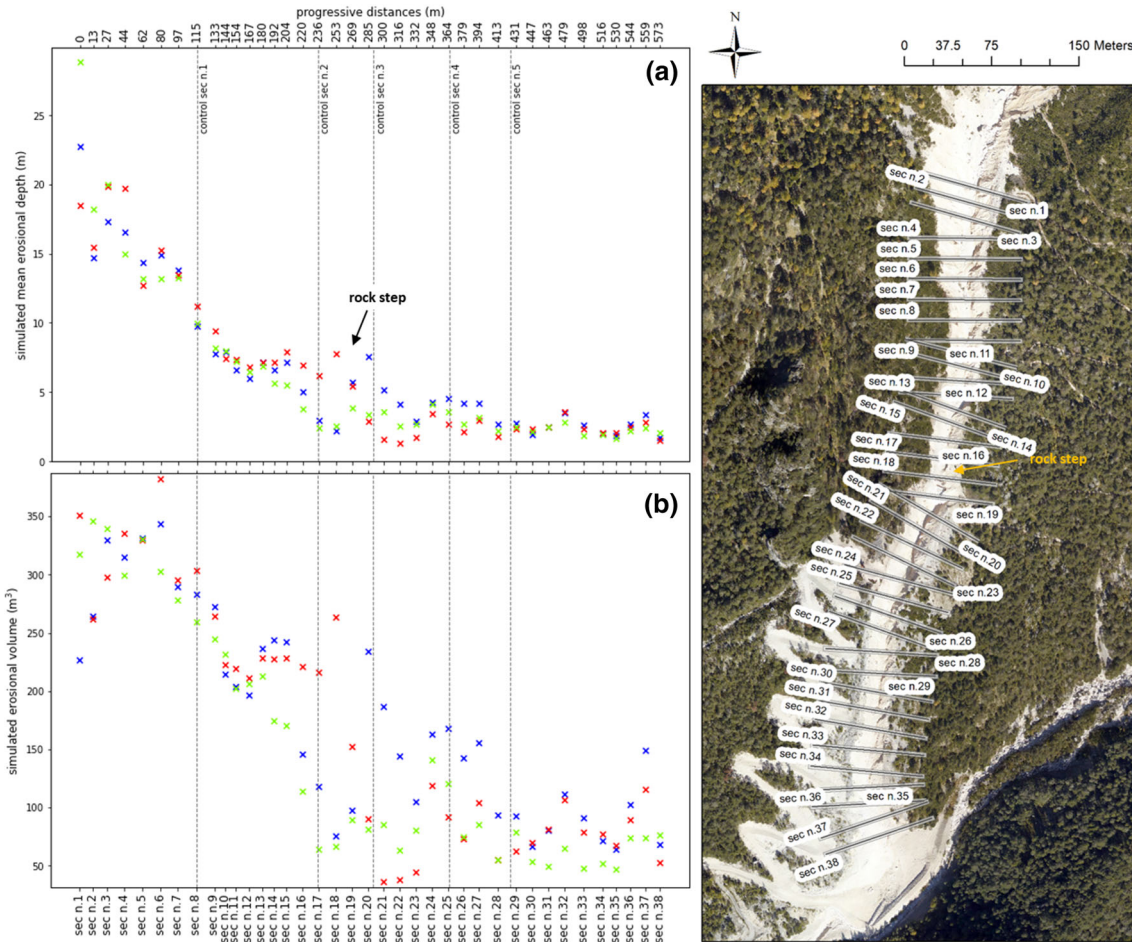


**FIGURE 12** Three hundred years return period model runs results in terms of (cross-section averaged) erosional depths (a) and (cross-section summarized) erosional volumes (b) simulated corresponding to thirty-eight, 2-m buffered inner domain cross-sections. *Note*: Blue, red and green colours represent the model runs corresponding to GNSS-, LiDAR- and UAV-derived DEMs, respectively
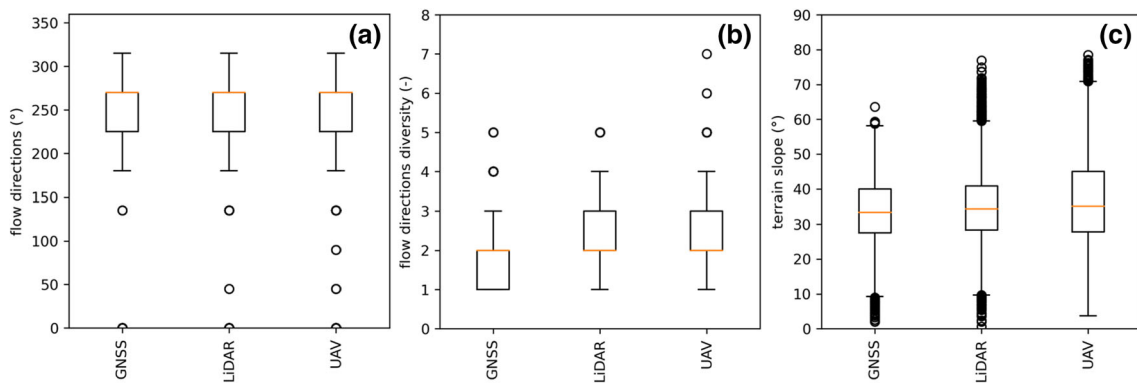


**FIGURE 13** Box plots of the flow direction (a), flow direction diversity (i.e. the number of unique flow direction values within a 3 × 3 moving window (b) and terrain slope (c) DEMs-derived raster-grids. *Note*: The analysed data refer to the envelope of modelled inundated areas during propagation

(i.e. arrival, ending and peak time) and peak discharges, for both the considered event scenarios.

The comparison among the model run plots corresponding to GNSS- and LiDAR-derived DEMs indicates that the most noticeable differences occur in the channel reach encompassing control cross-sections n.2 and n.3, where the corresponding DoD models show significant discrepancies between the two survey technologies (Figures 7a and d), mainly because of the inability of the terrestrial measurements-based DEM to properly reproduce complex gully features (i.e. rock step and steep gully banks).

These differences are related to an observable change in the simulated local flow dynamics corresponding to the massive rock step (Figure 1), approximately 300 m downstream of the model inlet section (Figure 10). In fact, just upstream of the rock step, the higher (cross-section averaged) erosional depths are modelled using the LiDAR-derived DEM as the input topographic surface (Figure 10a), with the simulated flow bifurcating into two principal flow paths (Figure 10c). Conversely, downstream of the rock step, higher (cross-section averaged) erosional depths are observed in the model run corresponding to the GNSS-derived DEM (Figure 10a), with the simulated flow following upstream a preferential flow line on the right and then downstream following a preferential flow line on the left (Figure 10b). Notably, the recognized change in the simulated local flow dynamics also affects the downstream channel reach encompassing control cross-sections n.4 and n.5, by determining minor discrepancies in the model run results even if no significant differences in the input topographic surfaces are observed.

This evidence is confirmed by Figures 11 and 12, along with Figures S6 and S7 in the online Supplementary Material. Regardless of the magnitude of the simulated event scenario, the plots clearly stress a change in the model behaviour related to the input topographic surface moving from upstream to downstream of the rock step, mainly in

the extent of the simulated erosional process (which represents the dominant geomorphic forcing within the study reach). The outlined model behaviour is strictly linked to the adopted schematization for the sediment entrainment–depositional process modelling. Indeed, it is simulated by assuming the channel bottom slope and flow velocity as controlling factors, both in turn depending on the digital topography.

On the other hand, the comparative analysis of the model run plots corresponding to the UAV-derived DEM indicates that noticeable differences affect almost the entire studied channel reach, mostly in terms of systematic 'under-estimation' of both mixture volume and peak discharge because of a modelled erosional process featuring an overall lower magnitude (Figures 8 and S4; Figures 9 and S5; Figures 10d, 11 and S6; Figures 12 and S7). To explain the recognized model behaviour, we focused on the value distributions of both the flow direction (computed as the steepest descent direction) and the terrain slope (computed along the flow direction) by only referring to the computational domain area actually affected by the flow (Figure 13). Indeed, regarding the employed routing model, these terrain attributes represent the main topographic parameters controlling both the solid–liquid mixture routing and sediment entrainment–depositional process. Overall, a comparison of Figure 13 plots indicates meaningful discrepancies among generated DEMs both in terms of modelled flow paths and topographic gradient, with the highest data variability shown by the UAV-based DEM derivatives likely due to the extremely high-topographic data source resolution. This evidence may represent the primary reason for the observed stronger control of the photogrammetrically reconstructed bathymetry on the simulated global flow dynamics.

A summary of the dispersion (i.e. maximum difference among the results of model runs of assigned return period) in the simulated mixture volumes and peak discharges for both considered event scenarios

**TABLE 3**   Maximum differences in simulated solid–liquid hydrograph volumes and peak discharges for 300-years return period model runs

| | Mixture volume | | | | |
| --- | --- | --- | --- | --- | --- |
| | Control sec n.1 | Control sec n.2 | Control sec n.3 | Control sec n.4 | Control sec n.5 |
| 'Absolute' differences (m$^3$) | 218.62 | 2574.15 | 3970.36 | 3202.45 | 3659.57 |
| 'Relative' differences (%) | 1.31 | 11.26 | 15.33 | 11.83 | 13.17 |
| | Peak discharge | | | | |
| | Control sec n.1 | Control sec n.2 | Control sec n.3 | Control sec n.4 | Control sec n.5 |
| 'Absolute' differences (m$^3$/s) | 5.98 | 18.40 | 12.54 | 11.39 | 15.42 |
| 'Relative' differences (%) | 12.06 | 24.25 | 15.36 | 15.33 | 20.44 |

*Note*: For each control cross-section, the 'relative' difference is computed as the percentage ratio between the 'absolute' difference and the mean of all corresponding simulated mixture volume and peak discharge values, respectivel

**TABLE 4**   Maximum differences in both the inundated areas during propagation and erosional–depositional volumes simulated at the computational domain scale for 300-years return period model runs

| | Inundated area (m$^2$) | Erosional area (m$^2$) | Erosional volume (m$^3$) | Depositional area (m$^2$) | Depositional volume (m$^3$) |
| --- | --- | --- | --- | --- | --- |
| 'Absolute' differences | 612.00 | 606.00 | 4072.13 | 168.00 | 793.25 |
| 'Relative' differences (%) | 6.27 | 11.85 | 15.58 | 3.62 | 15.73 |

*Note*: For each variable, the 'relative' difference is computed as the percentage ratio between the 'absolute' difference and the mean of all corresponding simulated values
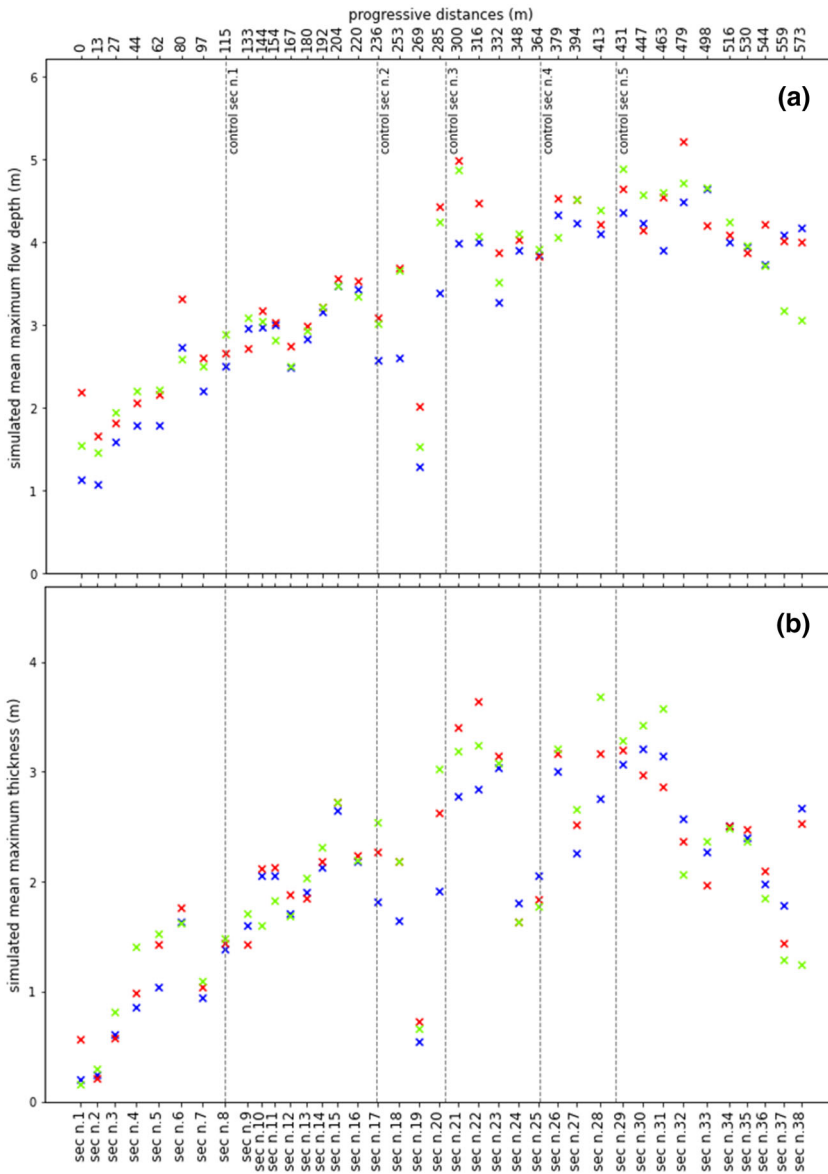
**FIGURE 14** Three hundred years return period model runs results in terms of (cross-section averaged) maximum flow depths (a) and thicknesses (b) simulated corresponding to inner domain cross-sections depicted in Figure 12. *Note*: Blue, red and green colours represent the model runs corresponding to GNSS-, LiDAR- and UAV-derived DEMs, respectively.

**TABLE 5** Minimum, maximum and average dispersion in simulated (cross-section averaged) maximum flow depth and thickness values for 300-years return period model runs

|  | Maximum flow depth (m) | Maximum thickness (m) |
|---|---|---|
| Min. 'absolute' differences | 0.06 | 0.02 |
| Max. 'absolute' differences | 1.12 | 1.42 |
| Avg. 'absolute' differences | 0.43 | 0.28 |
| Avg. 'relative' differences (%) | 12.62 | 16.69 |

*Note*: For both variables, the 'relative' differences are computed as the percentage ratio between the 'absolute' differences and the mean of all corresponding simulated (cross-section averaged) maximum values

is shown in Table 3 and Table S3 in the online Supplementary Material. Likewise, the maximum difference in both the inundated areas during propagation and erosional–depositional volumes modelled at the computational domain scale is summarized in Table 4 and Table S4 in the online Supplementary Material.

For both modelled event scenarios, the highest dispersion in the volumes of the simulated solid–liquid discharge hydrographs is observed at control cross-section n.3 (i.e. just downstream of the rock step; Figure 8), with ('relative') differences on the order of 15% of the mean of all corresponding simulated mixture volumes. Conversely, the best model run agreement (i.e. lowest dispersion in the simulation outcomes) is observed at control cross-section n.1 (i.e. approximately 100 m downstream of the model inlet section; Figure 8), with a global spread <5.10% of the mean of all corresponding simulated mixture volumes. Regarding the simulated hydrograph peak discharges, the highest dispersion in the 300- and 50-years return period model run outcomes is observed at control cross-sections n.2 and n.4, with ('relative') values up to 34.51% of the mean of all corresponding simulated peak discharges. In contrast, for both event scenarios, the best model run agreement is observed at control cross-section n.1, with a spread >10% of the mean of all corresponding simulated peak discharges. Furthermore, it is observed that the average 'relative' dispersion (i.e. mean of all computed 'relative' differences) in the simulated mixture hydrograph volumes is 10.58% (±5.42) and 10.77% (±3.61) for the 300- and 50-years return period model runs, respectively. On the other hand, the average 'relative' dispersion in the simulated
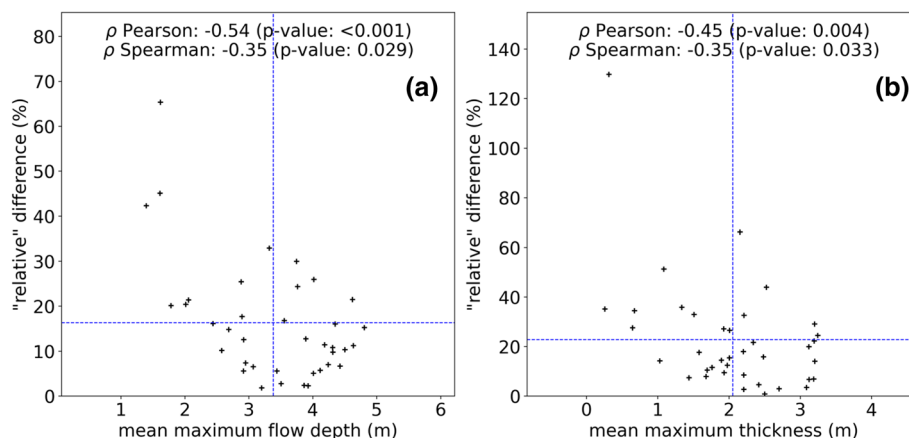
hydrographs peak discharges (17.49% [±4.82] and 24.54% [±8.51] for the 300- and 50-years return period model runs, respectively) is approximately double, thus highlighting a different influence of the topographic data source depending on the considered variable, regardless of the magnitude of the modelled event scenario. It is worth noting that both the mixture volume computation and wave peak detection are affected by the shape of the simulated solid–liquid discharge hydrograph, which in turn is controlled by the model output time step. In this research, the output time step was set to 10 s, as it proved to be a suitable value for ensuring a satisfactory smoothing of the numerical fluctuations while preserving the characteristic 'impulsive' shape of debris-flow hydrographs (Figures 8 and S4). On the other hand, it is also noted that the mixture hydrograph peak discharges were simply computed as the maximum of the corresponding simulated nonzero solid–liquid discharges vector. Therefore, the dispersion in the simulated hydrograph peak discharges was computed by comparing values not referring to the same time step. As a result of the outlined biases, an inherent uncertainty may affect the computed values.

By examining the data in Tables 4 and S4, regardless of the magnitude of the considered event scenario, the highest dispersion in the model run outcomes is observed in the simulated erosional volumes, with ('relative') differences up to 18.77% of the mean of all corresponding simulated volume values. In contrast, regarding the inundated areas during propagation, the ('relative') differences in the model run results are on the order of 6% of the mean of all corresponding simulated inundated area values, thus underpinning the different influence of the topographic data source on routing-modelling outcomes. However, this research focused on the routing modelling of a channelized debris flow. In the case of a non-channelized debris flow, a greater influence of the topographic data source on the simulated inundated areas may be expected, mainly due to the lower flow depths and velocities in turn enhancing the effect of the different shape 'complexity' of elevation models.

By referring to the flow depth and thickness, the plots in Figure 14 and Figure S8 in the Supplementary Material show the (cross-section averaged) maximum values simulated at the thirty-eight inner domain cross-sections (Figure 12) for the 300- and 50-years return period model runs, respectively. The corresponding dispersion values in the model run outcomes are summarized in Table 5 and Table S5 in the online Supplementary Material.

Overall, at the computational domain scale, the plots analysis indicates that the model runs corresponding to the GNSS-derived DEM

generally yielded lower (cross-section averaged) maximum values for both hydraulic variables, regardless of the return period of the event scenario. Interestingly, the plots also stress the absence of a meaningful relationship between the dispersion in the simulated (cross-section averaged) flow depth and thickness maximum values and variables magnitude, as confirmed by the scatter plots in Figure 15 and Figure S9 in the online Supplementary Material. In fact, Spearman's coefficient of the bivariate correlations is globally between −0.43 and 0.00 (−) with corresponding *p*-values higher than a test significance level equal to at least 0.05 (−), thus denoting a low to negligible statistical relationship.

Regarding the model run outcome differences (Tables 5 and S5), the dispersion in the simulated (cross-section averaged) maximum flow depths ranges from 0.06 to 1.12 m (inner domain cross-sections n.14 and n.38, respectively) and from 0.07 to 1.43 m (inner domain cross-sections n.24 and n.20, respectively) for the 300- and 50-years return period model runs, respectively. Likewise, the dispersion in the modelled (cross-section averaged) maximum thicknesses ranges from 0.02 to 1.42 m (inner domain cross-sections n.34 and n.38, respectively) and from 0.04 to 1.85 m (inner domain cross-sections n.19 and n.20, respectively) for the 300- and 50-years return period model runs, respectively. On the other hand, the average dispersion for both hydraulic variables is on the order of 0.30–0.40 m, regardless of the magnitude of the modelled event scenario. Therefore, despite the highlighted sensitivity of the employed routing model to the topographic data source, from a debris-flow risk planning and management point of view, these differences can be regarded as negligible overall for the case study of the Rovina di Cancia gully.

## 5 | CONCLUSIONS

In the proposed research, we initially assessed and compared the performances of both terrestrial- and aerial-based survey technologies widely used in the field of the numerical modelling of gravity-driven phenomena and suitable for characterizing the complex topography of a steep alpine debris-flow channel reach (i.e. GNSS, helicopter-based full-waveform LiDAR and UAV-based SfM digital photogrammetry). To accomplish this task, a combination of surface shape analysis, vertical quality assessment, spatially distributed modelling of vertical uncertainty and probabilistic differencing of (temporal concurrent) DEMs was used. Afterwards, we investigated the inherent influence of the topographic data source on the outcomes of a GIS-based cell

model for simulating stony debris flows by considering both high- and intermediate-magnitude flow conditions. In detail, we compared the results of the model runs carried out using the different interpolated topographic surfaces by focusing on those concerning the hazard, including: solid–liquid discharge hydrographs; areas inundated during propagation; erosional–depositional volumes; and erosional–depositional depths, maximum flow depths and maximum thicknesses.

By referring to the performances of tested survey technologies, both the quality analysis and spatially distributed elevation uncertainty modelling carried out on the derived DEMs indicated that both the GNSS and helicopter-based full-waveform laser altimetry technology can effectively be used to generate dense (i.e. high-resolution) and high-quality elevation models of debris-flow channels, also featuring low-magnitude uncertainty values corresponding to the channel bottom. Conversely, despite the absence of a statically significant doming deformation, the detected complex spatial pattern of the vertical error likely related to the strong topographic relief of the study site did not allow SfM-based digital photogrammetry to achieve comparable statistical performances. Overall, it appears that only the former survey technologies can actually provide a topographic characterization of the morphology of a debris-flow channel suitable for routing-modelling applications. However, the 'shape reliability' analysis of generated elevation models clearly stressed the inability of the terrestrial measurements-based DEM to properly reproduce the terrain features affecting gravity-driven flow dynamics (e.g. channel banks, steps and rugged areas), mostly due to the inherent limits of the survey technology (i.e. safety-related site accessibility issues, low density and non-uniform spatial arrangement of the measurements). On the other hand, the tested aerial-based survey technologies ensured a more faithful and finer representation of the gully shape, with the highest terrain 'complexity' observed in the photogrammetrically reconstructed surface, likely due to the extremely high topographic data source resolution.

Regarding the performed probabilistic differencing of DEMs exercises, this pointed out overall that although the compared survey techniques provide a comparable (i.e. not significantly different at 95% CI) digital representation of debris-flow channel bathymetry, meaningful discrepancies can be detected corresponding to morphologically complex terrain features (e.g. at rock steps), mainly due to the remarked inherent limits of terrestrial-based technology. In this context, this research also showed how, regardless of the magnitude of the considered flood event scenario, these topographic discrepancies have the potential to affect the simulated local flow dynamics, with model sensitivity to the topographic data source observed in most considered hydraulic and topographic variables (even if to a different extent). Furthermore, this research also stressed the primary role of the shape 'complexity' of the input bathymetry in controlling the global behaviour of the employed GIS-based cell routing model, mainly due to the adopted schematization for sediment entrainment–depositional process modelling.

Overall, despite the observed model sensitivity to the topographic data source, for the analysed channel reach, the recognized differences in the routing-modelling outcomes can be regarded as negligible from a risk planning and management point of view, thus suggesting that the topographic data source does not truly represent a determining factor in modelling applications of channelized debris-flow routing. However, the extrapolation of this research outcome must be done with care for at least three reasons. (1) The investigation was performed by focusing on a channelized debris flow. In the case of non-channelized debris flows, a different control of the topographic data source on the simulated flow dynamics may be expected, mainly due to the lower flow depths and velocities in turn enhancing the influence of the input elevation model shape 'complexity'. (2) The investigation was carried out on a confined debris-flow channel reach, mainly experimenting with entrainment processes. Different findings may be obtained by focusing on channelized debris flows involving different geomorphic forcings (i.e. sediment deposition or mixed sediment entrainment–depositional processes). (3) The use of either different rheological models or sediment entrainment–depositional process schematizations may lead to different research outcomes. Therefore, to improve the knowledge gained by this research, future investigations must be carried out on the outlined biases.

## CONFLICT OF INTEREST

The authors certify that they have no affiliations with (or involvement in) any organization or entity with any financial interest (such as honoraria; educational grants; participation in speakers' bureaus; membership, employment, consultancies, stock ownership, or other equity interest; and expert testimony or patent-licensing arrangements) or non-financial interest (such as personal or professional relationships, affiliations, knowledge or beliefs) in the subject matter or materials discussed in this paper. Furthermore, the authors declare that no conflict of interest exists with the suggested reviewers.

## DATA AVAILABILITY STATEMENT

GNSS data were acquired from the authors and are available upon request. Full-waveform LiDAR data were provided by the Veneto Region (Land Department, Cartography and Strategic Land Planning Section) by request of the authors and are not freely available. The UAV-derived images were provided by the Belluno Province (Department of Land Defence) by request of the authors and are not freely available. The authors wish to thank the Veneto Region (Land Department, Cartography and Strategic Land Planning Section) and the Belluno Province (Department of Land Defence) which provided the data used in the research.

## ORCID

*Mauro Boreggio* 🔟 https://orcid.org/0000-0001-9699-9338
*Martino Bernard* 🔟 https://orcid.org/0000-0001-8173-8805
*Carlo Gregoretti* 🔟 https://orcid.org/0000-0002-5855-9937

## REFERENCES

Aguilar, F.J., Agüera, F., Aguilar, M.A. & Carvajal, A.F. (2005) Effects of terrain morphology, sampling density, and interpolation methods on grid DEM accuracy. *Photogrammetric Engineering & Remote Sensing*, 71(7), 805–816. Available from: https://doi.org/10.14358/PERS.71.7.805

Alho, P., Hyyppä, H. & Hyyppä, J. (2009) Consequence of DTM precision for flood hazard mapping: A case study in SW Finland. *Nordic Journal of Surveying and Real Estate Research*, 6(1), 21–39. https://journal.fi/njs/article/view/2704.

Ali, M.D.A., Solomatine, D.P. & Di Baldassarre, G. (2015) Assessing the impact of different sources of topographic data on 1-D hydraulic modelling of floods. *Hydrology and Earth System Sciences*, 19(1), 631–643. Available from: https://doi.org/10.5194/hess-19-631-2015

Armanini, A., Fraccarollo, L. & Rosatti, G. (2009) Two-dimensional simulation of debris flows in erodible channels. *Computational Geosciences*, 35(5), 993–1006. Available from: https://doi.org/10.1016/j.cageo.2007.11.008

Bakuła, K., StĘpnik, M. & Kurczyński, Z. (2016) Influence of elevation data source on 2D hydraulic modelling. *Acta Geophysica*, 64(4), 1176–1192. Available from: https://doi.org/10.1515/acgeo-2016-0030

Bangen, S.G., Wheaton, J.M., Bouwes, N., Bouwes, B. & Jordan, C. (2014) A methodological intercomparison of topographic survey techniques for characterizing wadeable streams and rivers. *Geomorphology*, 206(2014), 343–361. Available from: https://doi.org/10.1016/j.geomorph.2013.10.010

Bernard, M., Boreggio, M., Degetto, M. & Gregoretti, C. (2019) Model-based approach for design and performance evaluation of works controlling stony debris flow with an application to a case study at Rovina di Cancia (Venetian Dolomites, Northeast Italy). *Science of the Total Environment*, 688, 1373–1388.

Berti, M. & Simoni, A. (2014) DFLOWZ: A free program to evaluate the area potentially inundated by a debris flow. *Computers & Geosciences*, 67(2014), 14–23. Available from: https://doi.org/10.1016/j.cageo.2014.02.002

Besl, p.J. & McKay, N.D. (1992) A method for registration of 3-d shapes. *IEEE Transactions on Pattern Analysis and Machine Intelligence*, 14(2), 239–256. Available from: https://doi.org/10.1109/34.121791

Bhuyian, M.N. & Kalyanapu, A. (2018) Accounting digital elevation uncertainty for flood consequence assessment. *Journal of Flood Risk Management*, 11, S1051–S1062. Available from: https://doi.org/10.1111/jfr3.12293

Boreggio, M., Bernard, M. & Gregoretti, C. (2018) Evaluating the differences of gridding techniques for digital elevation models generation and their influence on the modeling of stony debris flows routing: A case study from Rovina di Cancia basin (north-eastern Italian Alps). *Frontiers in Earth Science*, 6, 89. Available from: https://doi.org/10.3389/feart.2018.00089

Capra, L., Manea, V.C., Manea, M. & Norini, G. (2011) The importance of digital elevation model resolution on granular flow simulations: A test case for Colima volcano using TITAN2D computational routine. *Natural Hazards*, 59(2), 665–680. Available from: https://doi.org/10.1007/s11069-011-9788-6

Casas, A., Benito, G., Thorndycraft, V.R. & Rico, M. (2006) The topographic data source of digital terrain models as a key element in the accuracy of hydraulic flood modelling. *Earth Surface Processes and Landforms*, 31(4), 444–456. Available from: https://doi.org/10.1002/esp.1278

Cavalli, M. & Marchi, L. (2008) The effectiveness of airborne LiDAR's data in the recognition of channel-bed morphology. *Catena*, 75(3), 249–260. Available from: https://doi.org/10.1016/j.catena.2007.11.001

Cilloccu, F., Dequal, S., Brovelli, M.A., Crespi, M. & Lingua, A. (2009) *Ortoimmagini 1:10.000 e modelli altimetrici*. Linee Guida. Centro Interregionale per i Sistemi informatici, geografici e statistici: Roma.

Cook, A. & Merwade, V. (2009) Effect of topographic data, geometric configuration and modeling approach on flood inundation mapping. *Journal of Hydrology*, 377(1–2), 131–142. Available from: https://doi.org/10.1016/j.jhydrol.2009.08.015

Cucchiaro, S., Cavalli, M., Vericat, D., Crema, S., Llena, M., Beinat, A., Marchi, L. & Cazorzi, F. (2018) Monitoring topographic changes through 4D-structure-from-motion photogrammetry: Application to a debris-flow channel. *Environmental Earth Sciences*, 77(18), 632. Available from: https://doi.org/10.1007/s12665-018-7817-4

Egashira, S. & Ashida, K. (1987) Sediment transport in steep slope flumes. In *Proceedings of the ROC-Japan Joint Seminar on Water Resources*.

Erdogan, S. (2009) A comparison of interpolation methods for producing digital elevation models at the field scale. *Earth Surface Processes and Landforms*, 34(3), 366–376. Available from: https://doi.org/10.1002/esp.1731

Frank, F., McArdell, B.W., Huggel, C. & Vieli, A. (2015) The importance of entrainment and bulking on debris flow runout modeling: Examples from the Swiss Alps. *Natural Hazards and Earth System Sciences*, 15(11), 2569–2583. Available from: https://doi.org/10.5194/nhess-15-2569-2015

Gallay, M., Lloyd, C.D., McKinley, J. & Barry, L. (2013) Assessing modern ground survey methods and airborne laser scanning for digital terrain modeling: A case study from the Lake District, England. *Computers & Geosciences*, 51, 216–227. Available from: https://doi.org/10.1016/j.cageo.2012.08.015

Ghilardi, P., Natale, L. & Savi, F. (2001) Modeling debris-flow propagation and deposition. *Physics and Chemistry of the Earth, Part C*, 26(9), 651–656. Available from: https://doi.org/10.1016/S1464-1917(01)00063-0

Gomarasca, M.A. (Ed). (2009) *Basics of Geomatics*. Dordrecht: Springer 10.1007/978-1-4020-9014-1.

Gregoretti, C. & Dalla, F.G. (2008) The triggering of debris flow due to channel-bed failure in some alpine headwater basins of the Dolomites: Analyses of critical runoff. *Hydrological Processes*, 22(13), 2248–2263. Available from: https://doi.org/10.1002/hyp.6821

Gregoretti, C., Degetto, M., Bernard, M. & Boreggio, M. (2018) The debris flow occurred at Ru Secco Creek, Venetian Dolomites, on 4 August 2015: Analysis of the phenomenon, its characteristics and reproduction by models. *Frontier in Earth Sciences*, 6, 80. Available from: https://doi.org/10.3389/feart.2018.00080

Gregoretti, C., Degetto, M. & Boreggio, M. (2016) GIS-based cell model for simulating debris flow runout on a fan. *Journal of Hydrology*, 534, 326–340. Available from: https://doi.org/10.1016/j.jhydrol.2015.12.054

Gregoretti, C., Stancanelli, L.M., Bernard, M., Boreggio, M., Degetto, M. & Lanzoni, S. (2019) Relevance of erosion processes when modelling in-channel gravel debris flows for efficient hazard assessment. *Journal of Hydrology*, 568(Jan), 575–591. Available from: https://doi.org/10.1016/j.jhydrol.2018.10.001

Hengl, T. & Reuter, H.I. (Eds). (2009) *Geomorphometry: Concepts, Software, Applications*. Amsterdam: Elsevier.

Hensleigh, J. (2014) *Geomorphic change detection using multi-beam sonar*. MSc thesis, Utah State University.

Heritage, G.L., Milan, D.J., Large, A.R.G. & Fuller, I. (2009) Influence of survey strategy and interpolation model upon DEM quality. *Geomorphology*, 112(3–4), 334–344. Available from: https://doi.org/10.1016/j.geomorph.2009.06.024

Hodgson, M.E. & Bresnahan, P. (2004) Accuracy of airborne LiDAR-derived elevation. *Photogrammetric Engineering & Remote Sensing*, 70(3), 331–339. Available from: https://doi.org/10.14358/PERS.70.3.331

Höhle, J. & Höhle, M. (2009) Accuracy assessment of digital elevation models by means of robust statistical methods. *ISPRS Journal of Photogrammetry and Remote Sensing*, 64(4), 398–406. Available from: https://doi.org/10.1016/j.isprsjprs.2009.02.003

Höhle, J. & Potuckova, M. (2011) *Assessment of the Quality of Digital Terrain Models*. Neubrandenburg: European Spatial Data Research.

Hsieh, Y.-C., Chan, Y.-C. & Hu, J.-C. (2016) Digital elevation model differencing and error estimation from multiple sources: A case study

from the Meiyuan Shan landslide in Taiwan. *Remote Sensing*, 8(3), 199. Available from: https://doi.org/10.3390/rs8030199

Hurlimann, M., Copons, R. & Altimir, J. (2006) Detailed debris flow hazard assessment in Andorra: A multidisciplinary approach. *Geomorphology*, 78(3–4), 359–372. Available from: https://doi.org/10.1016/j.geomorph.2006.02.003

Hussin, H.Y., Quan, L.B., van Westen, C.J., Christen, M., Malet, J.P. & van Asch, T.W.J. (2012) Parameterization of a numerical 2-D debris flow model with entrainment: A case study of the Faucon catchment, Southern French Alps. *Natural Hazards and Earth System Sciences*, 12, 3075–3090. Available from: https://doi.org/10.5194/nhess-12-3075-2012

Isenburg, M. (2017) *LAStools – efficient LiDAR processing software*.

Jaboyedoff, M., Oppikofer, T., Abellán, A., Derron, M.H., Loye, A., Metzger, R. & Pedrazzini, A. (2012) Use of LiDAR in landslide investigations: A review. *Natural Hazards*, 61(1), 5–28. Available from: https://doi.org/10.1007/s11069-010-9634-2

James, M.R., Antoniazza, G., Robson, S. & Lane, S.N. (2020) Mitigating systematic error in topographic models for geomorphic change detection: Accuracy, precision and considerations beyond off-nadir imagery. *Earth Surface Processes and Landforms*, 45(10), 2251–2271. Available from: https://doi.org/10.1002/esp.4878

James, M.R. & Robson, S. (2012) Straightforward reconstruction of 3D surfaces and topography with a camera: Accuracy and geoscience application. *Journal of Geophysical Research*, 117(F3), F03017. Available from: https://doi.org/10.1029/2011JF002289

James, M.R. & Robson, S. (2014) Mitigating systematic error in topographic models derived from UAV and ground-based image networks. *Earth Surface Processes and Landforms*, 39(10), 1413–1420. Available from: https://doi.org/10.1002/esp.3609

Lane, S.N., Westaway, R.M. & Hicks, D.M. (2003) Estimation of erosion and deposition volumes in a large, gravel-bed, braided river using synoptic remote sensing. *Earth Surface Processes and Landforms*, 28(3), 249–271. Available from: https://doi.org/10.1002/esp.483

Lato, M.J., Hutchinson, D.J., Gauthier, D., Edwards, T. & Ondercin, M. (2014) Comparison of airborne laser scanning, terrestrial laser scanning, and terrestrial photogrammetry for mapping differential slope change in mountainous terrain. *Canadian Geotechnical Journal*, 52(2), 129–140.

Li, Z. (1993) Theoretical models of the accuracy of digital terrain models: An evaluation and some observations. *The Photogrammetric Record*, 14(82), 651–660. Available from: https://doi.org/10.1111/j.1477-9730.1993.tb00775.x

Lillesand, T.M., Kiefer, R.W. & Chipman, J.W. (2004) *Remote Sensing and Image Interpretation*, 5th edition. New York: Wiley.

Lindsay, J.B. (2016) Whitebox GAT: A case study in geomorphometric analysis. *Computers & Geosciences*, 95, 75–84. Available from: https://doi.org/10.1016/j.cageo.2016.07.003

Medina, V., Hurlimann, M. & Bateman, A. (2008) Application of FLATModel, a 2D finite volume code, to debris flows in the northeastern part of Iberian Peninsula: Experimental evidences and numerical modelling of debris flow initiated by channel runoff. *Landslides*, 5(1), 127–142. Available from: https://doi.org/10.1007/s10346-007-0102-3

Milan, D.J., Heritage, G.L., Large, A.R.G. & Fuller, I.C. (2011) Filtering spatial error from DEMs: Implications for morphological change estimation. *Geomorphology*, 125(1), 160–171. Available from: https://doi.org/10.1016/j.geomorph.2010.09.012

Miller, J.E. (1984) Basic concepts of kinematic-wave models. US Geological Survey Professional Paper, 1302.

Molina, J.L., Gonzalves, P.R., Molina, C., Aguilera, D.G. & Espejo, F. (2014) Geomatic methods at the service of water resources modelling. *Journal of Hydrology*, 509(2014), 150–162. Available from: https://doi.org/10.1016/j.jhydrol.2013.11.034

Moore, I.D. & Grayson, R.B. (1991) Terrain-based catchment partitioning and runoff prediction using vector elevation data. *Water Resources Research*, 27(6), 1177–1191. Available from: https://doi.org/10.1029/91WR00090

Passalacqua, P., Belmont, P., Staley, D., Simleym, J. & Arrowsmith, J.R. (2015) Analyzing high resolution topography for advancing the understanding of mass and energy transfer through landscapes: A review. *Earth-Science Reviews*, 148, 174–193. Available from: https://doi.org/10.1016/j.earscirev.2015.05.012

Pfeifer, N. (2005) A subdivision algorithm for smooth 3D terrain models. *ISPRS Journal of Photogrammetry and Remote Sensing*, 59(3), 115–127. Available from: https://doi.org/10.1016/j.isprsjprs.2004.09.002

Pourali, S., Arrowsmith, C. & Chrisman, N. (2014) Pourali S, Arrowsmith C, Chrisman N. 2014. Vertical accuracy assessment of LiDAR ground points using minimum distance approach. In *Research@Locate'14*, Canberra, Australia, 7–9 April, Winter S, Rizos C (eds). http://ceur-ws.org

R Development Core Team. (2008) *R: A Language and Environment for Statistical Computing*. Vienna: R Foundation for Statistical Computing. http://www.R-project.org

Reil, A., Skoulikaris, C., Alexandridis, T.K. & Roub, R. (2017) Evaluation of riverbed representation methods for 1D flood hydraulics model. *Journal of Flood Risk Management*, 11, 169–179.

Rickenmann, D., Laigle, B., McArdell, B.W. & Hubl, J. (2006) Comparison of 2D debris-flow simulation models with field events. *Computational Geosciences*, 10(2), 241–264. Available from: https://doi.org/10.1007/s10596-005-9021-3

Schaffrath, K.R., Belmont, P. & Wheaton, J.M. (2015) Landscape-scale geomorphic change detection: Quantifying spatially variable uncertainty and circumventing legacy data issues. *Geomorphology*, 250, 334–348. Available from: https://doi.org/10.1016/j.geomorph.2015.09.020

Scheidl, C. & Rickenman, D. (2010) Empirical prediction of debris-flow mobility and deposition fans. *Earth Surface Processes and Landforms*, 35, 157–173.

Scheidl, C., Rickenmann, D. & Chiari, M. (2008) The use of airborne LiDAR data for the analysis of debris flow events in Switzerland. *Natural Hazards and Earth System Sciences*, 8(5), 1113–1127. Available from: https://doi.org/10.5194/nhess-8-1113-2008

Sibson, R. (1981) A brief description of natural neighbor interpolation. In: Barnett, V. (Ed.) *Interpolating Multivariate Data*. New York: Wiley, pp. 21–36.

Simoni, A., Bernard, M., Berti, M., Boreggio, M., Lanzoni, S., Stancanelli, L. M. & Gregoretti, C. (2020) Runoff-generated debris flows: Observation of initiation conditions and erosion–deposition dynamics along the channel at Cancia (eastern Italian Alps). *Earth Surface Processes and Landforms*, 45(14), 3556–3571. Available from: https://doi.org/10.1002/esp.4981

Sodnik, J., Podobnikar, T. & Mikoš, M. (2012) Using LiDAR data for debris flow modeling. In *Proceedings of the 12th Congress INTERPRAEVENT*, Grenoble/France, pp. 573–583.

Takahashi, T. (1981) Debris flow. *Annual Review of Fluid Mechanics*, 13(1), 57–77. Available from: https://doi.org/10.1146/annurev.fl.13.010181.000421

Takahashi, T. (Ed.) (2007) *Debris Flow, Mechanics, Prediction and Countermeasures*. Leiden: Taylor & Francis/Balkema.

Tarboton, D.G. (2003) Terrain analysis using digital elevation models in hydrology. In *Proceedings of the 23rd ESRI International Users Conference*, San Diego, CA, July 7–11.

Tarolli, P. (2014) High-resolution topography for understanding Earth surface processes: Opportunities and challenges. *Geomorphology*, 216, 295–312. Available from: https://doi.org/10.1016/j.geomorph.2014.03.008

Taylor, J.R. (Ed.) (1997) *An Introduction to Error Analysis*, 2nd edition. Sausalito, CA: University Science Books.

Vosselman, G.V. & Maas, H.G. (Eds). (2010) *Airborne and Terrestrial Laser Scanning*. Dunbeath: Whittles.

Wackrow, R. & Chandler, J.H. (2008) A convergent image configuration for DEM extraction that minimises the systematic effects caused by an inaccurate lens model. *The Photogrammetric Record*, 23(121), 6–18. Available from: https://doi.org/10.1111/j.1477-9730.2008.00467.x

Wackrow, R. & Chandler, J.H. (2011) Minimising systematic error surfaces in digital elevation models using oblique convergent imagery. *The Photogrammetric Record*, 26(133), 16–31. Available from: https://doi.org/10.1111/j.1477-9730.2011.00623.x

Weng, Q. (2006) An evaluation of spatial interpolation accuracy of elevation data. In: Riedl, A., Kainz, W. & Elmes, G.A. (Eds.), *Progress in spatial data handling*. Berlin: Springer-Verlag, pp. 805–824.

Westoby, M., Brasington, J., Glasser, N.F., Hambrey, M.J. & Reyonds, M.J. (2012) Structure from Motion photogrammetry: A low cost effective tool for geoscience applications. *Geomorphology*, 179, 300–314. Available from: https://doi.org/10.1016/j.geomorph.2012.08.021

Wheaton, J.M. (2008) *Uncertainty in morphological sediment budgeting of rivers*. PhD thesis, University of Southampton.

Wheaton, J.M., Brasington, J., Darby, S.E. & Sear, D.A. (2010) Accounting for uncertainty in DEMs from repeat topographic surveys: Improved sediment budgets. *Earth Surface Processes and Landforms*, 35(2), 136–156.

Wilson, J.P. & Gallant, J.C. (2000) Digital terrain analysis. In: Wilson, J.P. & Gallant, J.C. (Eds.) *Terrain Analysis: Principles and Applications*. New York: Wiley, pp. 1–28.

Wilson, M.D. & Atkinson, P.M. (2005) The use of elevation data in flood inundation modelling: A comparison of ERS interferometric SAR and combined contour and differential GPS data. *International Journal of River Basin Management*, 3(1), 3–20. Available from: https://doi.org/10.1080/15715124.2005.9635241

Wood, J.D. (1996) *The geomorphological characterisation of digital elevation models*. PhD thesis, University of Leicester.

Wood, J.D. & Fisher, P.F. (1993) Assessing interpolation accuracy in elevation models. *IEEE Computer Graphics and Applications*, 13(2), 48–56. Available from: https://doi.org/10.1109/38.204967

Yang, X. & Hodler, T. (2000) Visual and statistical comparisons of surface modeling techniques for point-based environmental data. *Cartography and Geographic Information Science*, 27(2), 165–175. Available from: https://doi.org/10.1559/152304000783547911

## SUPPORTING INFORMATION

Additional supporting information may be found in the online version of the article at the publisher's website.